

Retrieving Near-Global Aerosol Loading over Land and Ocean from AVHRR

N. C. Hsu^{1,*}, J. Lee^{1,2}, A. M. Sayer^{1,3}, N. Carletta^{1,4}, S.-H. Chen^{1,4}, C. J. Tucker¹,
B. N. Holben¹, and S.-C. Tsay¹

¹NASA Goddard Space Flight Center, Greenbelt, MD, USA.

²Earth System Science Interdisciplinary Center, University of Maryland, College Park, MD, USA.

³Goddard Earth Sciences Technology and Research (GESTAR), Universities Space Research Association, Columbia, MD, USA.

⁴Science Systems and Applications, Inc., Lanham, MD, USA.

*Corresponding author: N. C. Hsu, NASA Goddard Space Flight Center, Greenbelt, MD, USA.
(Christina.Hsu@nasa.gov).

Abstract.

The spaceborne Advanced Very High Resolution Radiometer (AVHRR) sensor data record is approaching 40 years, providing a crucial asset for studying long-term trends of aerosol properties regionally and globally. However, due to limitations of its channels' information content, aerosol optical depth (AOD) data from AVHRR over land are still largely lacking. In this paper, we describe a new physics-based algorithm to retrieve aerosol loading over both land and ocean from AVHRR for the first time. The over-land algorithm is an extension of our Sea-viewing Wide Field-of-view Sensor (SeaWiFS) and Moderate Resolution Imaging Spectroradiometer (MODIS) Deep Blue algorithm, while a simplified version of our Satellite Ocean Aerosol Retrieval (SOAR) algorithm is used over ocean. We compare retrieved AVHRR AOD with that from MODIS on a daily and seasonal basis, and find in general good agreement between the two. For the satellites with equatorial crossing times within two hours of solar noon, the spatial coverage of the AVHRR aerosol product is comparable to that of MODIS, except over very bright arid regions (such as the Sahara), where the underlying surface reflectance at 630 nm reaches the critical surface reflectance. Based upon comparisons of the AVHRR AOD against Aerosol Robotic Network (AERONET) data, preliminary results indicate that the expected error confidence interval envelope is around $\pm(0.03+15\%)$ over ocean and $\pm(0.05+25\%)$ over land for this first version of the AVHRR aerosol products. Consequently, these new AVHRR aerosol products can contribute important building blocks for constructing a consistent long-term data record for climate studies.

1. Introduction

Success in the quest of quantifying anthropogenic impacts on global change accurately requires decades-long observations of atmospheric, oceanic, and land imaging from space. Analyses of the longest (nearly 40-year) daily record of imager data acquired by the Advanced Very High Resolution Radiometer (AVHRR) aboard the National Oceanic and Atmospheric Administration (NOAA) polar-orbiting meteorological satellites can contribute important building blocks toward this quest. The unique series of AVHRR measurements can be obtained from NOAA-7 (launched in 1981) to NOAA-19 (launched in 2009), comprised of data mainly from two different sensors: the AVHRR/2 instrument that spans from July 1981 to November 2000, followed by the AVHRR/3 to the present. To retrieve aerosol properties from both natural and anthropogenic sources, over both land and ocean, we need to first examine the mechanical, optical, and radiometric characteristics of the AVHRR sensors. These are discussed below.

AVHRR scans mechanically with $\pm 55^\circ$ from nadir and covers a swath width of 2,800 km. Although the native spatial resolution in local area coverage (LAC) mode is 1.1 km at the sub-satellite point, the actual pixel size and shape are somewhat dependent on scan angle. The LAC data are resampled at ~ 4 km spatial resolution to give a global area coverage (GAC) data set. Within each block of three across-track scan lines by five pixels along-track of LAC pixels, the first four pixels in the first scan line are averaged and the other eleven pixels are skipped. Thus, the AVHRR GAC data are a 4/15 partial sampling of every three by five pixel block, and fifteen being close to the square of four, are often referred to as '4 km' data. The GAC record for a 24-hour period (day and night) totals 0.6 GB, a large volume in the late 1970s but trivial today (Kidwell, 1997).

To fuel the mechanical complexity further, those satellites from NOAA-7 in July 1981 to NOAA-14 in 2000 were permitted to drift in orbit, where the drift or precession was two to three minutes per month in terms of later equatorial crossing times, in turn, introducing artifacts in AVHRR data (Kaufman et al., 2000; Tucker et al., 2005). Our previous results also indicate that this orbital drift imposes significant challenges in determining trends of aerosol loading over land and ocean due to changes in sampling spatial coverage with time (Hsu et al., 2012). Orbital drift was greatly minimized after the launch of NOAA-16 in 2000, and the viewing geometry information for these later sensors is provided within the Level 1 (L1B) input files. Thus, for processing the pre-NOAA K/L/M (or prior to NOAA-15) AVHRR data, we need to calculate the sun-target-sensor geometries directly from the orbital elements of the satellites. The orbital elements, including eccentricity, semi-major axis, inclination, location of ascending node, argument of periapsis, and the anomaly, are obtained from the Two-Line-Elements satellite attitude data source provided by the North American Aerospace Defense Command (*cf.* <https://www.celertrak.com/NORAD/documentation/tle-fmt.asp>).

The first AVHRR was equipped with four optical channels and was launched in October 1978 on TIROS-N. Subsequently, the sensor was improved to a 5-channel instrument (AVHRR/2, NOAA-7 through 14) and, for the most recent, 6-channel (AVHRR/3, NOAA-15 through 19). These bands are listed in Table 1, and their strengths and limitations for aerosol remote sensing are well-established (*cf.* Tanré et al., 1992; Mischenko et al., 1999 for detailed discussions). In brief, with only two overlapping spectral bands available on most sensors (channels 1 and 2 centered near 630 and 850 nm, *cf.* Figure 1, Table 1), the ability to infer aerosol type is very limited. The spectral width of channel 2 in particular is problematic, since it is a broad band which covers water vapor absorption lines, meaning that ancillary information about column water vapor content

is required to make quantitative use of this band. The AVHRR/3 sensors included a third solar band near 1.6 μm (channel 3a), which improves fine/coarse aerosol discrimination, although this band was inactive on many AVHRR sensors (either the 1.6 μm or 3.7 μm channels were in operation, not both simultaneously), and as such is not considered further at the present time to improve sensor-to-sensor consistency. AVHRR/3 also had the advantage that channels 1 and 2 were narrower and did not significantly overlap compared to the spectral responses of these bands on AVHRR/2 instruments (*cf.* Figure 1). Differences between the sensors' spectral response functions make the task of achieving multi-sensor consistency less straightforward. The remaining three bands (channels 3b, 4, and 5), centered near 3.7, 11, and 12 μm , are more similar between the AVHRR/2 and AVHRR/3 series sensors, and are of great utility for applications such as surface/cloud temperature monitoring and detection of thermally-active aerosols (e.g., mineral dust, volcanic ash). Since AVHRR/1 on TIROS-N and NOAA-6 has only 4 channels and lacks the 12 μm band, which is needed for our Deep Blue algorithm, AVHRR measurements before the year 1981 will not be considered.

Despite these limitations, AVHRR data have been used for retrieving aerosol optical depth (AOD) by various groups. Most AOD data sets created from AVHRR measurements are over-water only, since water surface reflectance in this spectral region is low and can be modeled with reasonable accuracy as a function of near-surface wind speed. One-channel algorithms such as described in Rao et al. (1989) and Stowe et al. (1997) use the 630 nm band (avoiding the difficulties of water vapor absorption in channel 2) but are then restricted to assuming a single aerosol optical model everywhere, which leads to type-dependent AOD biases. Two- or three-channel approaches (e.g., Rao et al., 1989; Mishchenko et al., 1999; Ignatov and Stowe, 2002; Ignatov et al., 2004) permit retrieval of AOD and Ångström exponent (AE), thus providing some indication of aerosol

size, although the sensitivity to size remains small and there is essentially no sensitivity to other parameters such as aerosol absorption. Validation of earlier AVHRR data sets is limited due to the sparse availability of ground-truth data at these times, although a few, mostly regional, studies have been performed (e.g. Stowe et al. 1997, Haywood et al. 2001, Zhao et al. 2002, 2003, 2004). Other studies have focused on more statistical long-term comparisons with Sun photometers rather than instantaneous matchups (Liu et al., 2004), or on comparison of overlapping AVHRR time series to assess sensor-to-sensor consistency (Ignatov et al., 2004).

Several attempts have also been made to use AVHRR to determine AOD over land, for which characterization of land surface reflectance presents a significant difficulty. Knapp and Stowe (2002) proposed a method using Aerosol Robotic Network (AERONET, Holben et al., 1998) to estimate the surface reflectance in the vicinity of individual sites, and then constructing surface reflectance models as a function of land cover type. Riffler et al. (2010) take a 45-day window and essentially use a minimum reflectance technique (with an additional stratification by viewing zenith angle) to estimate surface reflectance for a given location. Mei et al. (2014) used ancillary surface information from the Moderate Resolution Imaging Spectroradiometer (MODIS) in concert with the AVHRR 3.7 μm band (which is comparatively unaffected by the presence of aerosols) and Normalized Difference Vegetation Index (NDVI, Tucker, 1979) to infer surface reflectance over China. In all cases, aerosol optical models are prescribed rather than retrieved, due to the limited information content of the measurements. More recently, synergistic use of AVHRR with other instruments on board the MetOp platforms has enabled improved retrieval of AOD over both land and ocean (EUMETSAT, 2016). The combination of sensors provides additional information content for identification of aerosol type, and discrimination between clouds and heavy aerosols, which ameliorates some of the issues of AVHRR-only algorithms.

As a result of these obstacles, it has been a highly challenging task to retrieve aerosols globally from AVHRR, particularly over land. Nevertheless, AVHRR instruments provide valuable measurements from 1981 to the present, a time series which is otherwise not available from US Earth Observing System (EOS) sensors. Based upon previous results from our Sea-viewing Wide Field-of-view Sensor (SeaWiFS) Deep Blue aerosol products, we demonstrated that an algorithm based on NDVI using a pair of red and near infrared channels (e.g., 650 and 865 nm, close to AVHRR channels 1 and 2) can be useful in determining surface reflectance over vegetated land when shortwave infrared channels (such as 2.1 μm) are lacking (Hsu et al., 2013). In order to take advantage of this nearly 40-year long-term time series of AVHRR records, we develop a new approach, which is a modified version of the Deep Blue algorithm, to retrieve aerosol properties from AVHRR over land and ocean with similar data structures following the convention of our SeaWiFS aerosol products. Over ocean the Satellite Ocean Aerosol Retrieval (SOAR) algorithm, which has been applied to SeaWiFS and Visible Infrared Imaging Radiometer Suite (VIIRS) measurements (Sayer et al., 2012a, 2017a), is likewise adapted for use with AVHRR to complement Deep Blue by providing coverage over water surfaces. Like SeaWiFS, as AVHRR LAC data are not available everywhere, we use the GAC data in retrieval processing for consistency between satellite platforms.

Sensor radiometric calibration plays a key role in constructing long-term climate data records. This is particularly important for this study, since there is no onboard solar band calibration for AVHRR. Various approaches have been applied to characterize the absolute calibration and on-orbit degradation of the instruments. This first version of the AVHRR Deep Blue data products uses the calibration of Vermote and Kaufman (1995), which is also used for NASA's long-term NDVI time series data products (e.g. Tucker et al., 2005). Vermote and

Kaufman (1995) provide a methodology for the absolute calibration of AVHRR bands 1 and 2, which is repeated through time to monitor and correct for the degradation of these bands on-orbit. A first step uses views of high-altitude bright clouds as ‘white’ reference targets to provide a relative calibration between the two bands. A second step determines an absolute calibration of channel 1, using off-nadir pixels over ocean where the aerosol load is low and Rayleigh signal comparatively high. This absolute channel 1 calibration can then be transferred to channel 2 using the cloud-derived relative calibration between these bands. Other methodologies have been explored (e.g., Heidinger et al., 2002; Wu et al., 2010; Bhatt et al., 2016), and the use of their calibrations will be investigated for future versions.

In this paper, we describe the details of this new extension of our Deep Blue/SOAR algorithms to AVHRR. Section 2 summarizes the methodology of the over-land and over-water algorithms, and detailed changes made in each key component compared to the other applications of Deep Blue and SOAR. Section 3 illustrates the results of the daily and seasonal aerosol products generated from the new algorithms and their comparisons with those from MODIS. Finally, we show provisional validation of the new AVHRR Deep Blue products in Section 4, followed by some conclusions in Section 5. This paper focuses primarily on the discussion of retrieval algorithms, while a detailed evaluation of the AVHRR Deep Blue aerosol product performance using AERONET and other measurements is provided by a companion paper, Sayer et al. (2017b). In this study, we use data from AVHRR/2 on NOAA-14 and AVHRR/3 on NOAA-18 to demonstrate its capability of processing both older and newer AVHRR instruments, although this algorithm can be applied to other AVHRR sensors from NOAA-7 to NOAA-19 as well. AVHRR AOD data have been processed using these algorithms for parts of the NOAA-11, NOAA-14, and

NOAA-18 missions; more information, including download links, can be found at <https://deepblue.gsfc.nasa.gov>.

2. Descriptions of AVHRR Aerosol Retrieval Algorithm

To retrieve AVHRR aerosol properties over land and ocean, we employ the Vector Linearized Discrete Ordinate Radiative Transfer (VLIDORT; Spurr, 2006) radiative transfer model to compute the reflected intensity field, which is defined by

$$R(\mu, \mu_0, \phi) = \frac{\pi I(\mu, \mu_0, \phi)}{\mu_0 F_0}, \quad (1)$$

where R is the normalized radiance (or apparent reflectance), F_0 is the extra-terrestrial solar flux, I is the radiance at the top of the atmosphere (TOA), μ is the cosine of the view zenith angle, μ_0 is the cosine of the solar zenith angle, and ϕ is the relative azimuth angle between the direction of propagation of scattered radiation and the incident solar direction. This radiative transfer code includes full multiple scattering and takes into account polarization. Using VLIDORT, lookup tables (LUTs) were generated based upon the spectral response functions of a given AVHRR sensor (*cf.* Figure 1) for different solar/viewing geometries and underlying surface (land and ocean) boundary conditions for aerosol retrievals.

However, before the retrieval, the AVHRR TOA reflectances must first be corrected for absorption by ozone, water vapor, and well-mixed gases (details described by Sayer et al., 2017a). For this initial version of the data set, gas absorption coefficients from Ignatov and Stowe (2002) for NOAA-15 were used (since these values are close to average of those reported by that study for NOAA-11, -14, and -18), scaled to account for total column ozone and water vapor read in from the MERRA2 reanalysis (Bosilovich et al., 2015). In addition, for our over-water retrievals, near-surface wind speed from MERRA2 is used to take into account the effects of oceanic

whitecaps and Sun-glint strength adequately, as in prior applications of SOAR (Sayer et al., 2012a, 2017a). After the gas absorption correction, the processing stream is subsequently split into land or ocean algorithm, according to the MODIS land/sea mask, to account for the underlying surface boundary conditions in the LUTs. Advantages of MERRA2 include that it is available for the whole AVHRR record, which enables consistency between processing of different AVHRR sensors, and is at a higher spatial resolution (0.625° longitude, 0.5° latitude) than some other reanalyses.

2.1 Land Algorithm (Deep Blue)

Similar to our SeaWiFS/MODIS algorithm, before the aerosol retrieval is performed, we first screen out the pixels contaminated by the presence of clouds. Due to the lack of the blue bands and $1.38\ \mu\text{m}$ cirrus channel for AVHRR, the previous MODIS cloud screening module has been modified to account for the band differences. The schematic diagram of the AVHRR Deep Blue cloud screening scheme is depicted in Figure 2. We utilize all of the bands that are available for both AVHRR/2 and AVHRR/3 from visible to thermal infrared wavelengths to fully take advantage of the spectral information provided by the AVHRR sensor for detecting clouds. As shown in Figure 2, instead of using the $412\ \text{nm}$ channel (available to MODIS and SeaWiFS), a spatial variability filter based on the TOA reflectance at $630\ \text{nm}$ (R_{630}) within a 3×3 pixel area is employed for AVHRR. Also, in order to account for the dynamic range of surface reflectances at $630\ \text{nm}$ over different ecosystem types, different threshold values are applied over darker and brighter surfaces. Based upon our extensive tests, this method is robust in filtering out puffy (e.g. cumulus) clouds as well as cloud edges. Checks on brightness temperature (BT) at $11\ \mu\text{m}$ (BT11) have been implemented in conjunction to BT difference (BTD) between 11 and $12\ \mu\text{m}$ (BTD11-12) tests to effectively detect high or optically-thin clouds. Finally, in order to distinguish the heavy

dust plumes from clouds, we also adopt a heavy dust flag so that the processing stream will bypass the cloud screening module when this is triggered (i.e., $\text{BTD}_{11-12} < -1.5$ K). These thresholds are empirical, adapted for AVHRR from our prior implementation of Deep Blue to MODIS (e.g. Hsu et al., 2013).

The aerosol optical models used in our AVHRR algorithm are in general consistent with those in the MODIS and SeaWiFS Deep Blue algorithm (*cf.* Hsu et al., 2004, 2013 for details). However, there have been a number of changes made in our AVHRR surface reflectance determination scheme to accommodate the channel differences between AVHRR and SeaWiFS/MODIS. These changes are summarized below.

2.1.1 Determination of Surface Reflectance

As demonstrated in our previous results (Hsu et al., 2013), the calculation of surface reflectance plays a key role in the accuracy of the retrieved aerosol properties. Since AVHRR has limited channels compared to later, more advanced sensors such as SeaWiFS and MODIS, the previous Deep Blue surface reflectance determination scheme needs to be modified. Figure 3 depicts the flowchart of our AVHRR surface reflectance estimation module. The details of each component are described as follows:

2.1.1.1 Deep Blue Surface Database

For urban, dry, and transitional land surfaces, similar to the SeaWiFS/MODIS applications, a database method is used for determining surface reflectance. This was compiled based upon the minimum reflectivity method at 0.1° resolution for each season using AVHRR TOA reflectance at 630 nm (*cf.* Hsu et al., 2004 for details). In brief, this approach is designed to seek the minimum

Rayleigh-corrected TOA reflectance for a certain period of time at each location, and uses this as a proxy for surface reflectance. In order to construct a surface database for AVHRR, we first apply various tests to filter out pixels contaminated by the presence of clouds using cloud screening scheme described above. Reflectances which pass these tests are then corrected for the contribution from molecular (Rayleigh) scattering and averaged into a daily mean for a given grid cell. Finally, the surface reflectance values in the AVHRR database are calculated by a second-order polynomial fit through the lowest 15 percentile of points in a given grid cell against the scattering angles of these observations; the scattering angle (Θ) is defined as

$$\Theta = \cos^{-1}(-\cos \theta_0 \cos \theta + \sin \theta_0 \sin \theta \cos \phi) \quad (2)$$

where θ_0 , θ , and ϕ are the solar zenith, sensor view zenith, and relative azimuth angles, respectively. These angular curve fittings of surface reflectance are performed for each NDVI group ($\text{NDVI} < 0.18$, $0.18 \leq \text{NDVI} < 0.35$, or $\text{NDVI} \geq 0.35$) collected in the given grid cell, provided that a sufficient sample size (20 or more points) is acquired. Based on prior experience with SeaWiFS and MODIS, this approach and fit type was found to be able to accurately capture the main angular variations in surface reflectance.

Figure 4 shows the derived global 630 nm surface reflectance maps for NOAA-18 AVHRR, based upon five years (2006-2010) of AVHRR data, for each season using the above approach. Due to limited AVHRR channels and information content the surface database is constructed over both land and ocean in order to help identify the turbid water for the SOAR algorithm (Section 2.2). For the AVHRR over-land algorithm, the surface reflectance is determined using the database approach over moderately bright arid and urban regions where 630 nm surface reflectance is between 0.15 and 0.30 (Figure 3). As discussed in e.g. Hsu et al. (2004)

and Seidel and Popp (2012), aerosol signals diminish when the surface reflectance reaches the critical surface reflectance; for the 630 nm wavelength this includes many arid and semi-arid regions, such as parts of the Sahara Desert and Arabian Peninsula, as well as snow/ice-covered land. Over these types of surfaces, we cannot accurately retrieve aerosol properties using measurements from single-view satellite sensors with this wavelength. However, 630 nm surface reflectances over arid regions in China and Mongolia are not as bright as those in the Sahara and Arabian Peninsula, and are in general less than 0.30 (Figure 4). Consequently, we exclude pixels over the deserts and semi-deserts in North Africa for retrievals, but include those over dry regions in China and Mongolia where the surface reflectance at 630 nm is below the critical values and thus suitable for aerosol retrievals. Finally, if BTD11-12 is more negative than -1.5 K, AOD retrieval will be performed regardless of surface condition, since for thick dust plumes the majority of the satellite signal comes from atmosphere. Figure 5 shows the geographic regions where different approaches are used for surface reflectance. As described above the database method is used over urban, dry, or transitional land surfaces, while a NDVI method (introduced below) is used over vegetated areas.

2.1.1.2 Vegetated Land Surfaces

The phenological cycle of vegetation (growth and senescence) means that the reflectance of vegetated surfaces can vary rapidly, particularly compared to barren surfaces such as deserts. Therefore, it is important to determine surface reflectance at a high temporal resolution to minimize errors in AOD related to changing surface characteristics. In this regard, the AVHRRs have a weakness compared to the MODIS and VIIRS sensors, in that the latter two include shortwave infrared (SWIR) bands, useful for estimating surface characteristics on an instantaneous basis, which AVHRR lacks.

SeaWiFS has a similar limitation. However, based upon our previous SeaWiFS Deep Blue retrievals, we found that the NDVI can serve as a useful proxy to estimate surface reflectance, making it possible to instantaneously derive surface reflectance and thus AOD in both blue (490 nm) and red (670 nm) bands (Hsu et al., 2013; Sayer et al., 2012b). Although the 670 nm AOD showed an AOD-dependent underestimation, the 490 nm AOD, which showed negligible bias, could be used to correct the 670 nm AOD. For AVHRR, our preliminary investigations (not shown) suggested that the NDVI approach resulted in a more significant bias in 630 nm AOD than SeaWiFS. Since there is no additional band in AVHRR to correct for the bias (unlike SeaWiFS), we have developed a modified NDVI-based method to determine surface reflectance for AVHRR, which merge the use of NDVI with the concept of minimum reflectance approach used in our Deep Blue surface database construction mentioned above.

Although similar to the minimum reflectance technique, this method utilizes NDVI rather than TOA reflectance when determining the ‘clean’ background condition. The Rayleigh-corrected NDVI ($NDVI_{RC}$) is defined as

$$NDVI_{RC} = \frac{R_{RC,band2} - R_{RC,band1}}{R_{RC,band2} + R_{RC,band1}}, \quad (3)$$

where $R_{RC,band1}$ and $R_{RC,band2}$ are Rayleigh-corrected TOA reflectances in bands 1 (630 nm) and 2 (850 nm), respectively. The use of NDVI is to avoid extra dimensions for observation geometry when deriving surface reflectance, thereby minimizing the search window. Since the surface reflectance is strongly dependent on observation geometry, the minimum reflectance only represents surface reflectance for the specific observation geometry for which the minimum reflectance is observed. Figure 6 shows AVHRR Rayleigh-corrected TOA reflectance in band 1 and $NDVI_{RC}$ for two consecutive orbits on a relatively clean day over the U.S. The $NDVI_{RC}$ exhibits

a much smaller dependence on observation geometry than the Rayleigh-corrected TOA reflectance indicating that ‘clean’ conditions (i.e. cloud-free, low AOD) can be chosen by compositing only temporal samples for NDVI, in contrast to needing both temporal and angular samples for the TOA reflectance. This is because the ratio in the NDVI definition decreases the angular dependence of the signal.

Consequently, the surface database is created by searching for maximum NDVI (as maximum NDVI corresponds to minimum band 1 surface reflectance) in each 30-day temporal window and $0.1^\circ \times 0.1^\circ$ grid box. The dates of the maximum NDVI are also stored to interpolate (linearly) the NDVI values for the dates in between. The surface reflectance in band 1 ($R_{sfc,band1}$) can then be calculated as

$$R_{sfc,band1} = \frac{1-NDVI_{database}}{1+NDVI_{database}} R_{rc,band2}, \quad (4)$$

where $NDVI_{database}$ is the maximum NDVI stored in the database. As can be inferred from Eq. (4) the angular dependence of the 630 nm surface reflectance is described by the instantaneous 850 nm TOA reflectance in this approach. Figure 7 shows the 30-day maximum NDVI database created for the year 2006 and four day of year (DOY) windows 1-30, 91-120, 181-210, and 271-300, representative for boreal winter, spring, summer, and fall, respectively. The seasonal variation and spatial pattern of NDVI indicate reliability of a 30-day window. We also investigated (not shown) temporal windows between 10 and 45 days, although neither showed superior performance over the 30-day window in every aspect. Shorter temporal windows tended toward an underestimation in AOD due to the remaining aerosol signal in the NDVI database, while longer temporal windows tended toward overestimation by choosing more densely vegetated conditions than representative for the bulk of the period.

Since the NDVI database is susceptible to the residual aerosol signal on the day chosen for the database, an aerosol correction needs to be applied to the database to alleviate the aforementioned underestimation in AOD. To this end, atmospheric correction is performed for AVHRR band 1 and band 2 TOA reflectances to derive atmosphere-corrected (for both Rayleigh and aerosol contributions) NDVI, denoted $NDVI_{Ac}$, and compare with $NDVI_{Rc}$. AVHRR observations are collocated with AERONET sites over North America for the period from 2006 to 2011 with a spatial window of 0.1° in latitude and longitude and a temporal window of 30 min. Then, the atmospheric contribution to TOA reflectance is removed using radiative transfer calculations utilizing the AERONET-observed spectral AOD as input. For AERONET, cloud-screened and quality-assured Level 2 direct Sun measurements (Smirnov et al., 2000; Holben et al., 2006) were used, and AOD at AVHRR band 1 and 2 were derived from the spectral AOD and AE over the 440-870 nm wavelength range. The comparison between $NDVI_{Ac}$ and $NDVI_{Rc}$ provides useful information for the aerosol correction scheme.

Figure 8 shows differences between $NDVI_{Ac}$ and $NDVI_{Rc}$ as a function of 550 nm AOD, $NDVI_{Rc}$, air mass parameter ($AMP, \sec\theta_o \times \sec\theta_v$), and scattering angle, which are factors on which the aerosol signal is dependent. Also shown are the differences after applying corrections for aerosol signals described here. The NDVI differences before the corrections reveal that the aerosol contamination in the $NDVI_{Rc}$ is strongly dependent on AOD and results in negative biases. Relatively weak dependences are also found on NDVI, AMP, and scattering angle. It should be noted that in addition to the strong dependence on AOD, the absolute difference between $NDVI_{Rc}$ and $NDVI_{Ac}$ generally increases with increasing NDVI and decreasing scattering angle up to $\sim 120^\circ$. The dependence on AMP is less significant. This is because both increasing NDVI and decreasing scattering angle enhance the aerosol signal at a given AOD, due to increasing contrast between

aerosol and surface signals, and increasing aerosol scattering intensity, respectively. By the same reasoning, a dependence on AMP is also expected (due to increasing aerosol signal with air mass), but the dependence is much smaller than those of the other parameters. This is likely due to the contextual characteristics of the bias and sensitivity.

Trial and error based on the median differences between $NDVI_{RC}$ and $NDVI_{Ac}$ leads us to the following correction equations:

For scattering angle $\geq 120^\circ$,

$$NDVI_{RC,corrected} = NDVI_{RC} + [0.23 + 0.15 \times (AMP - 1)] \times AOD_{550} \times NDVI_{RC} \quad (5)$$

For scattering angle $< 120^\circ$,

$$NDVI_{RC,corrected} = NDVI_{RC} + [0.23 + 0.15 \times (AMP - 1) + 0.03 \times (120^\circ - \Theta)] \times AOD_{550} \times NDVI_{RC} \quad (6)$$

It is found that these corrections significantly improve the medians and central 68% intervals of the NDVI differences (i.e. medians closer to zero and spread of distribution smaller).

In actual implementation, since ‘true’ background AOD values are not available for each location and time, a monthly AOD climatology (one value for each of the 12 calendar months, not one value for each month of the satellite record) is created using the Aqua MODIS Collection 6 Deep Blue AOD product. Specifically, the 5th percentiles of 13-year Level 3 daily AOD record from 2003 to 2015 in each $1^\circ \times 1^\circ$ grid were chosen to represent the background AOD and used to correct the NDVI database using Eqs. (5) or (6) depending on scattering angle. It should be noted that the climatology was created in a way to correct the NDVI database a marginal amount, such that the different spatial resolution between the NDVI database (0.1°) and AOD climatology (1°) did not generate a noticeable checkerboard pattern in the spatial distribution of AOD. Likewise, it is expected that the use of a single monthly climatology for the entire AVHRR record would not

lead to significant biases. Note that this does not mean that the MODIS Deep Blue record ‘feeds in’ to the AVHRR record on an instantaneous basis, only to correct the background AOD for the NDVI database calculation as described above. Other aerosol data sets could in principle be used to create this background AOD climatology instead. In this way the actual AVHRR AOD retrieval remains largely independent of the MODIS Deep Blue AOD retrieval.

The performance of the surface reflectances derived from the NDVI database is evaluated by comparing against the atmospherically-corrected TOA reflectances calculated above. Here data with 550 nm AOD from AERONET < 0.2 are only compared to minimize uncertainties in the atmospheric correction procedure. As shown in Figure 9, the NDVI database-derived surface reflectances (estimated surface reflectances) are well-correlated with the atmosphere-corrected TOA reflectances (benchmark surface reflectances) in general, showing root-mean-square error (RMSE) ranging from 1.70% to 2.67% and mean bias (MB) from -0.38% to -0.92% (excluding winter due to the small number of data points). This performance is more than acceptable given the fact that the surface reflectances for AVHRR are from a database at a 30-day temporal resolution rather than instantaneous values (although interpolated between nodes). The outliers (with low number density) are largely due to this temporal limitation of the database approach. These outliers are from a few locations at which the database method is less optimal, and thus would not significantly affect a large-scale view of the aerosol product. For instance, AERONET sites located near croplands, such as Bondville (Illinois, U.S.) and Egbert (Ontario, Canada), and near complex environment, such as Billerica (near Boston, U.S.) contribute to a large portion of the outliers. It should be noted that in the Level 2 aerosol data product the effect of the outliers, especially due to spatial inhomogeneity, would be mitigated by the spatial aggregation (2×2

pixels), as Figure 9 compares data at different spatial resolutions (0.1° for the surface database, L1B resolution for the benchmark).

The application of our NDVI-based land algorithm is limited to certain surface and viewing geometry conditions, due to the use of single 630 nm band in retrieving AOD. Through extensive investigation on retrieval sensitivities and error characteristics of AOD, we have chosen the following procedures to select retrieval pixels for this approach:

i) 630 nm surface reflectance is lower than 0.15, and International Geosphere-Biosphere Programme (IGBP) land cover type (Friedl et al., 2010) is not classified as ‘open shrublands’, ‘grasslands’, or ‘croplands’. Because AOD retrieval sensitivity decreases with increasing surface reflectance, data are excluded when surface reflectance is too high.

ii) If IGBP land cover type falls into the three categories in i), air mass factor needs to be higher than 2.5 in addition to the surface reflectance criterion for the pixel to be eligible for retrieval. It is found that AOD retrieved over these three land cover types are less accurate compared to that over other land cover types, mainly due to higher surface reflectance values (although less than 0.15) and higher uncertainty of estimating surface reflectance over these regions. This requires the additional filter to only include data with high signal-to-noise ratio, which reduces artificial hotspots resulting from errors in calculated surface reflectance combined with weak aerosol signal.

2.1.2 AOD Determination and Extrapolation to 550 nm

After the surface reflectance is determined based upon surface types as described above, a maximum likelihood method is used with pre-calculated LUTs to match the appropriate values of AOD to the measured reflectances from AVHRR, based on these surface reflectances and the aerosol optical models as used for other satellite sensors (Hsu et al., 2004). This is the same basic

approach as used for SeaWiFS/MODIS Deep Blue, except for the different available spectral bands. Note that the 630 nm band is used for the inversion, and thus the retrieved AOD is also at 630 nm. For details of the algorithm see Hsu et al. (2004, 2013).

Since 550 nm AOD is the primary product of the Deep Blue algorithm for other satellite sensors, and is widely used within the aerosol community, the 630 nm AOD is extrapolated to 550 nm using an AE climatology. This saves the data user from having to perform such an extrapolation themselves. The climatology is created from the full Level 2 AERONET record available at the present time. Specifically, multi-year monthly median 440-870 nm AE values at each AERONET site are calculated based on daily median values, when the numbers of data points are higher than 5 for both the daily and monthly calculations. The monthly climatology is then expanded globally to a $1^\circ \times 1^\circ$ grid using exponentially weighted means of the medians from the AERONET sites. For the weighting factor, e-folding lengths of 500 km for longitude and 250 km for latitude are used (to account for prevailing zonal winds over the globe). It was found that the background AOD from AERONET can be accurately interpolated regardless of the e-folding length in the range of 100-1000 km (Zhang et al., 2016), although the error can increase over areas where AERONET sites are sparsely distributed. It should be noted that the single channel retrieval of AVHRR leads us to using a seasonal aerosol optical model in each geographic region rather than retrieving it in each pixel, such that extrapolation of AOD using the optical models is not optimal.

2.2 Ocean Algorithm (SOAR)

The over-water AOD retrieval is based on the same SOAR algorithm applied previously to SeaWiFS and VIIRS observations, simplified to account for the more limited measurement

capabilities of the AVHRR sensors. Full details of SOAR are provided by Sayer et al. (2012a, 2017a), and a summary of key points is below.

2.2.1 Selection of Suitable Pixels

Pixels contaminated by Sun-glint, clouds, or suspected of excessively turbid water are excluded from processing; Sun-glint masking is as described in Sayer et al. (2012a) but cloud and turbid water masks are different due to the different spectral bands available to AVHRR. Pixels are identified as cloudy if they are either bright (band 1 TOA reflectance > 0.08), cold ($12\text{ }\mu\text{m BT} < 270\text{ K}$), or heterogeneous (3×3 pixel standard deviation of TOA reflectance > 0.005 for either band 1 or band 2). To minimize contamination from undetected cloud or 3D effects, pixels adjacent to a pixel identified as cloudy are also excluded. These thresholds have been determined empirically and tested to ensure both few false negatives (i.e., undetected cloud) and positives (i.e., over-screening of aerosol plumes).

Pixels are identified as persistently turbid (or potentially land-contaminated) and excluded if the seasonal Deep Blue surface reflectance database value at 630 nm is above 0.06 (Section 2.1.1.1). This typically removes 0-2 pixels on some coastlines, except for areas of larger-scale turbidity such as the Bay of Bengal or mouth of the Amazon River. If such pixels are not excluded then the effect is a positive bias in retrieved AOD, as AVHRR unfortunately has insufficient information content to easily distinguish between turbid water and elevated aerosol loading.

2.2.2 Pixel-Level Retrieval

As with prior applications of SOAR (Sayer et al., 2012a, 2017a), individual pixels are used to retrieve aerosol properties in a multispectral weighted least-squares fit of observed TOA reflectances against pre-computed values stored in LUTs. The SeaWiFS and VIIRS applications

simultaneously retrieved the AOD at 550 nm and fine mode fraction (FMF) as well as the best-fit aerosol optical model (which consists of bimodal size distribution parameters and spectral complex refractive index), from which other parameters like AE can be derived in a self-consistent manner. As only two measurements are available for AVHRR, only the AOD and best-fit aerosol optical model are retrieved and the FMF is fixed for each aerosol optical model. The LUT is generated with the VLIDORT radiative transfer code (Spurr, 2006) and aerosol model information is provided in Table 2 (including references for optical model parameters). Use of these models keeps a level of consistency with other applications of SOAR: other over-ocean AOD retrievals for AVHRR typically retrieve AOD and AE but assume the same aerosol size distribution/refractive index globally (e.g., Mishchenko et al., 1999; Ignatov and Stowe, 2002), which is a slightly different approach to aerosol ‘typing’. To allow some more flexibility in distinguishing low-AOD conditions between open oceans and continental outflow regions, where FMF may be different (e.g., Smirnov et al., 2011), there are two maritime models with different FMF permitted (but otherwise the same AOD range and modal optical properties). Different LUTs are calculated for each AVHRR sensor, as their central wavelengths and bandwidths are different (e.g., Tanré et al., 1992).

The ocean surface reflectance model used is described in Sayer et al. (2017a), which is an updated version of that from Sayer et al. (2012a), incorporating more recent measurements of optical characteristics of water and pigments. A \log_{10} chlorophyll concentration (mg m^{-3}) of -0.5 is assumed, although the surface reflectance over AVHRR bands is only weakly dependent on this over the range of typical oceanic chlorophyll concentrations. As such this approximation should add negligible (<0.01) additional uncertainty in retrieved AOD.

The retrieval minimizes the sum of the squared deviation between measurements and LUT values, weighted by assumptions of the uncertainty in the AVHRR bands (from calibration, gas correction, and the forward model), providing essentially a χ^2 statistic referred to as the retrieval cost. At present these relative uncertainties are assumed to be 3% for band 1 and 20% for band 2; this deweighting of band 2 is to account for the greater calibration and gas absorption uncertainties with this band. As a result the AOD is mostly determined by band 1, while band 2 provides some constraint on best-fit aerosol optical model. In version 1 of the AVHRR data set, the TOA reflectances have also been scaled for NOAA-14 (by 0.95 and 0.89 for bands 1 and 2) and NOAA-18 (by 0.97 and 0.95) based on validation against AERONET and examination of maps of aerosol model choices. This is an empirical step taken as a first-pass to decrease potential systematic uncertainties related to the sensor calibration used and trace gas absorption, which will hopefully be improved upon for future versions once the different available multi-sensor AVHRR calibrations have been evaluated for aerosol processing. Note that the NASA NDVI products which also use the Vermote and Kaufman (1995) calibration methodology also apply further empirical corrections, although at the NDVI stage rather than the level 1 stage (Tucker et al 2005, and references therein), so such adjustments are not unprecedented.

2.3 Aggregation to 2×2 Cell Resolution and Quality Flags

Over both land and ocean, after the retrieval, the AOD and other parameters are aggregated to 2×2 ‘cell’ resolution, which is the output resolution for the Level 2 product, and corresponds to approximately $8.8 \times 8.8 \text{ km}^2$ horizontal pixel size at the sub-satellite point (although see prior discussion on LAC/GAC sampling). The median of all retrieved quantities is taken (to reduce sensitivity to, e.g., any residual cloud contamination) from the up to 4 available pixels. Over ocean, the aerosol model with the lowest cell-average cost is chosen as the ‘best’ solution, and this is

reported in the Level 2 product. The main retrieved quantity is the AOD at 550 nm and AVHRR band 1; over ocean, related information derived from the aerosol optical model (AOD at AVHRR band 2, FMF, and AE) are also provided.

Following the convention used in MODIS/SeaWiFS Deep Blue products, the quality assurance (QA) flags in AVHRR Level 2 data also have 4 different levels where QA=0 indicates no retrieval, QA=1 indicates a possible problem with retrieval, and 2/3 indicate moderate and high quality (i.e., no reason to suspect a problem) respectively. Note that over ocean there is no QA=2 category. Over ocean, a cell is assigned QA=3 if the retrieval cost is less than 5 (i.e. a good fit between measurements and forward-modeled reflectances was obtained), at least 2 (out of 4) pixels within the cell were used in the retrieval, and the AOD standard deviation in the cell is less than 1. In practice the requirement for at least 2 out of 4 pixels is the most restrictive. Over land, the AOD standard deviation requirement is stricter (0.35 and 0.20 for QA=2 and 3, respectively), due to the greater difficulty in AOD retrieval over land, and the pixel count requirement is the same as over ocean. Since potentially there still could be cloud contamination in the QA=1 cells, only QA=2 or 3 cells are propagated into Level 3 aggregated data, and in general only QA=2 or 3 retrievals should be used for most applications.

3. Results and Discussions

Figure 10 illustrates one of the examples of our AVHRR AOD products and its comparison with MODIS Aqua over South America as well as the surrounding water on September 7, 2006. For MODIS, over-land data from the Deep Blue algorithm are used (Hsu et al., 2013; Sayer et al., 2013). Over water, the Dark Target MODIS ocean retrieval product (Tanré et al., 1997; Levy et al., 2013) is used, as SOAR has not yet been applied to MODIS. Our newly developed AVHRR

algorithm, shown in Figure 10 (c), extends the spatial coverage of current AVHRR AOD products, which are only available over water, to the land surface types. The AVHRR data shown here are based upon measurements from NOAA-18 with a local solar equator crossing time of ~2:00 pm, which is slightly later than the 1:30 pm equator crossing time for Aqua. Nevertheless, the areas of high AOD in our AVHRR image correspond well to the smoke plumes visible in the MODIS true-color image, capturing the heavy smoke transported southward. We also compare the AOD values at 550 nm derived from our AVHRR data with those based upon the MODIS/Aqua aerosol retrievals for the corresponding day, as shown in Figure 10 (b). The results indicate that the AOD values from these two sensors are quite comparable, despite their differences in observation time.

We also examined algorithm results over Asia, which often exhibits the most complex aerosol conditions observed, with a mixture of dust and fine mode pollution particles. One such example, shown in Figure 11, is for April 16, 2006. On this day, a transported dust plume observed over western and central China around 40° N, 80°–114° E occurred as a result of a springtime dust outbreak event over the Taklamakan Desert as well as Inner Mongolia. While this plume was well captured by our AVHRR data, the spatial coverage is sparser over arid regions around 40° N, 80°–105° E compared to the MODIS data. This is due to the use of air mass filter applied to the AVHRR retrievals over arid areas. East of this dust plume, the region was covered by widespread fine mode pollution extending all the way to the East China Sea and the Yellow Sea; the elevated AVHRR AOD values over this area reflect this.

In addition to the daily data, we also compare the AVHRR and MODIS products on the seasonal basis. Figure 12 provides the maps of seasonal averaged AOD from both AVHRR (NOAA-18) and MODIS (Aqua). These composites were created by taking daily Level 3 products, and then averaging these first to monthly, and then monthly to seasonal, time steps. To stop poorly-

sampled grid cells from introducing potentially significant sampling error into the comparison, a daily grid cell was considered valid for an instrument if it contained at least 5 retrievals passing QA checks, and a grid cell was considered valid on a monthly basis if it contained at least 3 valid days. These thresholds are somewhat subjective but, particularly for cloudy regions, provide a reasonable balance between data coverage and sampling representivity.

As shown in Figure 12, both AVHRR and MODIS reproduce the same major spatial and seasonal variations in aerosol loading. For example, there were intense wild fires over Siberia, in the summer of 2006, producing heavy smoke plumes all the way into the Arctic Ocean, as seen in the retrieved June-July-August AOD maps from both sensors. The patterns of elevated aerosol loading due to anthropogenic air pollution in East Asia and South Asia are also clear in both sensors throughout the year. The seasonal north-south movement of the Saharan dust transport displayed in the AVHRR maps is also in agreement with that in the MODIS maps. More detailed comparisons with the MODIS aerosol products are provided in the companion paper, Sayer et al.(2017b).

Seasonal means can be influenced by sampling frequency of the given dataset. AVHRR and MODIS sensors have (to a first order) similar swath widths and similar Level 2 pixel sizes, so it would be expected that sampling frequencies would be similar. Figure 13 confirms that on a general basis this is indeed the case, and also reinforces the extent to which cloud cover, snow/ice, and polar night can limit coverage from all instruments of these types (many grid cells have fewer than 25% of days providing data within a season). Overall AVHRR coverage, while sharing similarities to that of MODIS, is often around 10% less frequent. This is due to the more limited information content of the sensor, meaning that cloud screening and QA checks are stricter in AVHRR to minimize the chances of poor-quality retrievals propagating into the data product.

Coverage in the Sahara and Arabian Peninsula is also limited or absent in AVHRR, as this surface is too bright in most cases to perform an AOD retrieval from this type of sensor from the available bands (Section 2.1.1). In AVHRR coverage-sparse regions such as this, sampling differences are also therefore likely to be playing a role in differences in the seasonal AOD observed by the two sensors.

Figure 14 shows a comparison of multiannual mean AOD at 550 nm from our NOAA18 AVHRR, SeaWiFS (version 4), and MODIS Aqua (Collection 6) aerosol products for their common overlap period (2006-2010). Note the MODIS ocean data are from the standard Dark Target group ocean product (Levy et al., 2013); otherwise, all land data shown are Deep Blue, and ocean data are SOAR. Similar patterns in the mean AOD are seen in all data sets. MODIS has the highest coverage; AVHRR has more gaps due to the sensor's limitations at discerning the aerosol signal over the brightest desert surfaces, as discussed, as well as the more conservative cloud screening (due to more limited spectral channels) reducing coverage over tropical forests. SeaWiFS has similar cloud-screening limitations due to a lack of any thermal IR bands. SeaWiFS also, at this point, represents the oldest of the three Deep Blue algorithm versions and has some additional coverage gaps because of this (Sayer et al. 2012b; Hsu et al. 2013). Some differences in AOD magnitudes result, as in the seasonal comparisons above, from these sampling differences.

Over water, the AVHRR and SeaWiFS data are quite comparable. Validation exercises have shown that both have near-zero biases in open-ocean conditions, and slight negative biases in high-AOD conditions (Sayer et al. 2012a, 2017b). Over ocean MODIS shows the same spatial patterns but with a generally higher AOD. As noted, this is not from the SOAR algorithm. The standard MODIS Collection 6 over-ocean AOD product is known to have a positive bias in low-AOD conditions (of order 0.01-0.02; Sayer et al. 2012d, Levy et al. 2013), and a more variable

positive bias in dust-laden conditions due to the lack of a non-spherical dust optical model (e.g. Mishchenko et al., 1997, Levy et al., 2003, Banks et al., 2017, Lee et al., 2017). Therefore, these patterns are broadly consistent with the known characteristics of each data set. Additional comparisons are provided in the comparison data set evaluation paper, Sayer et al. (2017b).

4. Validation against AERONET AOD

Figure 15 shows scatter density plots providing a global summary of the validation of AVHRR retrievals based upon 6 years (2006-2011) of NOAA-18 data and 5 years (1995-1999) of NOAA-14 data over land and ocean. For NOAA-18 a total of 40 sites contributed to over-ocean data, and 427 over land data; for NOAA-14 the numbers are 20 and 123 respectively. Because there are fewer AERONET sites before the year 2000, fewer matchup data points are found for NOAA-14 compared to those for NOAA-18. Full details of the validation are provided by Sayer et al. (2017b), but a summary is given here. AVHRR and AERONET data are compared using the standard technique of averaging satellite data within 25 km of the AERONET site and AERONET data within 30 minutes of the satellite overpass, to decrease the effect of spatiotemporal sampling differences. The AERONET direct-Sun Version 2 Level 2 (cloud-screened and quality assured; Smirnov et al., 2000) data products are used. This comparison shows results for AVHRR band 1 AOD (near 630 nm). AERONET does not measure this wavelength directly, so the bands are interpolated spectrally, which adds negligible additional uncertainty to the approximate 0.01 AOD uncertainty of the AERONET direct-Sun measurement.

For both NOAA-18 and -14 AVHRR data, the correlation coefficients are high in all cases, and the median biases fairly small. The statistic f indicates the fraction of points matching AERONET within the expected error (EE), an envelope of $\pm(0.03+15\%)$ over ocean and

$\pm(0.05+25\%)$ over land for this first version, on global average for both surface types. While the exact sensitivity to various assumptions is quite dependent on the context of each individual retrieval (i.e. aerosol loading and type, surface cover type, solar/view geometry, etc), these EE envelopes provide a guideline first-order expectation of retrieval performance. They are based on prior applications of the Deep Blue and SOAR algorithms, and the known limitations of the AVHRR sensors (cf. Rao et al., 1989; Tanré et al., 1992; Mishchenko et al., 1999, Hsu et al. 2004, 2013; Sayer et al. 2012a,b, 2017b). Specifically, proportion of retrievals within the expected error calculated separately for regions over ocean, vegetated land only and entire land are 73.9%, 77.0%, and 73.5% (NOAA-18) and 64.3%, 79.4% and 73.9% (NOAA-14), respectively. Uncertainties over ocean are smaller than those over land, due in large part to the darker surface signal. Over land, performance is better when the data are subset to show only vegetated matchups, for the same reason. These results demonstrate the applicability of the Deep Blue and SOAR algorithms to AVHRR measurements.

5. Conclusion

To understand the effects of aerosols on climate and human health, satellite observations are crucial in providing continuous temporal and spatial sampling of aerosol properties from source to sink regions for such studies. With the advent of the EOS-era sensors in the late 1990s, an accurate long-term aerosol dataset from these well-calibrated satellite measurements became possible. However, for many climate studies the EOS data records are not always of sufficient length to adequately address the question of long-term aerosol changes on regional/global scales. Therefore, results using earlier satellite sensors such as AVHRR, which provide nearly 40 years of measurements, are highly desirable in order to extend the dataset for use in these studies. This earlier time period (from 1981 to 2000) before the launch of EOS satellites is particularly important

for understanding changes in the levels of aerosol loading over Asia, where a large fraction of global economic growth over the past several decades has occurred.

In this paper, we demonstrated a new approach to quantitatively retrieve, for the first time, this much needed aerosol information from AVHRR over land and ocean on a global scale. Our approach is an extension of the SeaWiFS/MODIS Deep Blue and SOAR aerosol algorithms. Over land, we merge the use of NDVI with the framework of the minimal reflectance method to account for the effects of changing vegetation in surface reflectance. Over ocean, a simplified version of SOAR is employed for aerosol retrieval. Using these algorithms, our results show that daily, seasonal, and annual distributions of AOD from AVHRR are in reasonable agreement with those from MODIS, despite the limitations on its information content. The cloud screening scheme for AVHRR is also shown to be robust in distinguishing heavy aerosol plumes from clouds, based upon the results of intercomparing daily AOD data from AVHRR and MODIS.

Extensive comparisons have also been performed between the AOD values retrieved from the AVHRR instruments on NOAA-14 and -18 and the AERONET data. Using the calibration of Vermote and Kaufman (1995), our AVHRR AOD values show good agreement with the AERONET data over land and ocean for both the NOAA-14 (1995-1999) and NOAA-18 (2006-2011) time periods. Based upon these comparisons, the expected error is estimated to be $\pm(0.03+15\%)$ over ocean and $\pm(0.05+25\%)$ over land for this first version of AVHRR aerosol products. Detailed evaluations of the AVHRR products are included in a companion paper (Sayer et al., 2017b). For the next step, we plan to process the AVHRR time series by employing different calibrations (e.g., Heidinger et al., 2002; Wu et al., 2010; Bhatt et al., 2016) to examine the sensor-to-sensor consistency using the multiple overlapping years of data in order to ensure the long-term stability of the aerosol data records.

Multiple years of the AVHRR Deep Blue aerosol products from NOAA-11, -14 and -18 are now available via the Deep Blue project web site (<https://deepblue.gsfc.nasa.gov>). This dataset will eventually be able to provide nearly 40 years of aerosol data records from AVHRR not only over ocean, but also over the entire cloud-free, snow/ice-free land area, except for very bright desert regions such as the Sahara and arid regions in the Arabian Peninsula. When combined with data from EOS-era sensors such as SeaWiFS and MODIS, our AVHRR record will provide a critical piece in the construction of a consistent long-term aerosol data record for deriving aerosol trends on both global and regional scales.

Acknowledgements

This work was supported by the NASA Radiation Sciences Program, managed by Dr. Hal Maring. The AVHRR Deep Blue data described in this work are freely available to download from <https://portal.nccs.nasa.gov/datashare/AVHRRDeepBlue/>. Data hosting resources were provided by the NASA High-End Computing (HEC) Program through the NASA Center for Climate Simulation (NCCS) at Goddard Space Flight Center. NOAA L1B GAC data were obtained from <https://www.class.ncdc.noaa.gov>. MERRA2 data were obtained from NASA's Goddard Earth Sciences Data and Information Services Center (<https://disc.gsfc.nasa.gov>). We would also like to express our gratitude to AERONET site PIs (<https://aeronet.gsfc.nasa.gov>) in establishing and maintaining the long-term stations used in this investigation. The authors thank three anonymous reviewers for their helpful suggestions.

References

- Banks, J. R., H. E. Brindley, G. Stenchikov, and K. Schepanski (2017), Satellite retrievals of dust aerosol over the Red Sea and the Persian Gulf (2005–2015), *Atmos. Chem. Phys.*, 17, 3987–4003, doi:10.5194/acp-17-3987-2017.
- Bhatt, R., D. R. Doelling, B. R. Scarino, A. Gopalan, C. O. Haney, P. Minis, and K. M. Bedka (2016), A Consistent AVHRR Visible Calibration Record Based on Multiple Methods Applicable for the NOAA Degrading Orbits. Part I: Methodology, *J. Atmos. Ocean Tech.*, 33, 2499–2515, doi:10.1175/JTECH-D-16-0044.1.
- Bosilovich et al. (2015), MERRA-2: Initial Evaluation of the Climate, Technical Report Series on Global Modeling and Data Assimilation, NASA/TM–2015-104606/Vol. 43, <https://gmao.gsfc.nasa.gov/pubs/tm/docs/Bosilovich803.pdf> [Accessed 08 December 2016].
- Choi, M. J. Kim, J. Lee, M. Kim, Y.-J. Park, U. Jeong, W. Kim, H. Hong, B. Holben, T. F. Eck, C. H. Song, J.-H. Lim, and C.-K. Song (2016), GOCI Yonsei Aerosol Retrieval (YAER) algorithm and validation during the DRAGON-NE Asia 2012 campaign, *Atmos. Meas. Tech.*, 9, 1377–1398, doi:10.5194/amt-9-1377-2016.
- EUMETSAT (2016), Polar Multi-Sensor Aerosol Product: User Guide, V2, available online at http://www.eumetsat.int/website/wcm/idc/idcplg?IdcService=GET_FILE&dDocName=PDF_PMAP_PG&RevisionSelectionMethod=LatestReleased [Accessed 17 November 2016].
- Friedl, M. A., D. Sulla-Menashe, B. Tan, A. Schneider, N. Ramankutty, A. Sibley, and X. Huang (2010), MODIS Collection 5 global land cover: Algorithm refinements and characterization of new datasets, *Remote Sens. Environ.*, 114, 168–182, doi:10.1016/j.rse.2009.08.016.
- Haywood, J. M., P.N. Francis, I. Geogdzhayev, M. Mishchenko, and R. Frey (2001), Comparison of Saharan dust aerosol optical depths retrieved using aircraft mounted pyranometers and 2-channel AVHRR algorithms, *Geophys. Res. Lett.*, 28, 2393–2396, doi:10.1029/2000GL012625.
- Heidinger, A. K., C. Cao, and J. T. Sullivan (2002), Using Moderate Resolution Imaging Spectrometer (MODIS) to calibrate advanced very high resolution radiometer reflectance channels, *J. Geophys. Res.*, 107(D23), 4702, doi:10.1029/2001JD002035.
- Holben, B. N., T. F. Eck, I. Slutsker, D. Tanre, J. P. Buis, A. Setzer, E. Vermote, J. A. Reagan, Y. J. Kaufman, T. Nakajima, F. Lavenu, I. Jankowiak, and A. Smirnov (1998), AERONET: A federated instrument network and data archive for aerosol characterization, *Remote Sens. Environ.*, 66, 1–16, doi:10.1016/S0034-4257(98)00031-5.
- Holben, B. N., T. F. Eck, I. Slutsker, A. Smirnov, A. Sinyuk, J. Shafer, D. Giles, and O. Dubovik (2006), AERONET's version 2.0 quality assurance criteria, *Proc. SPIE*, 6408, 64080Q, doi:10.1117/12.706524.

- Hsu, N. C., S. C. Tsay, M. D. King, and J. R. Herman (2004), Aerosol properties over bright-reflecting source regions, *IEEE Trans. Geosci. Remote Sens.*, 42, 557–569, doi:10.1109/TGRS.2004.824067.
- Hsu, N. C., R. Gautam, A. M. Sayer, C. Bettenhausen, C. Li, M. J. Jeong, S.-C. Tsay, and B. N. Holben (2012), Global and regional trends of aerosol optical depth over land and ocean using SeaWiFS measurements from 1997 to 2010, *Atmos. Chem. Phys.*, 12, 8037–8053, doi:10.5194/acp-12-8037-2012.
- Hsu, N. C., M.-J. Jeong, C. Bettenhausen, A. M. Sayer, R. Hansell, C. S. Seftor, J. Huang, and S.-C. Tsay (2013), Enhanced Deep Blue aerosol retrieval algorithm: The second generation, *J. Geophys. Res. Atmos.*, 118, doi:10.1002/jgrd.50712.
- Ignatov, A., and L. Stowe (2002), Aerosol Retrievals from Individual AVHRR Channels. Part I: Retrieval Algorithm and Transition from Dave to 6S Radiative Transfer Model, *J. Atmos. Sci.*, 59, 313–334, doi: 10.1175/1520-0469(2002)059<0313:ARFIAC>2.0.CO;2.
- Ignatov, A., J. Sapper, S. Cox, I. Laszlo, N. R. Nalli, and K. B. Kidwell (2004), Operational Aerosol Observations (AEROBS) from AVHRR/3 On Board NOAA-KLM Satellites, *J. Ocean. Atmos. Tech.*, 21, 3–26, doi: 10.1175/1520-0426(2004)021<0003:OAOAFO>2.0.CO;2.
- Kaufmann, R.K., Zhou, L., Knyazikhin, Y., Shabanov, N., Myneni, R. and Tucker, C.J. (2000), Effect of orbital drift and sensor changes on the time series of AVHRR vegetation index data. *IEEE Transactions on Geoscience and Remote Sensing* 38:2584–2597, doi:10.1109/36.885205.
- Kidwell, K.B. (1997). Polar Orbiter Data Users' Guide (TIROS-n, NOAA-6, NOAA-7, NOAA-8, NOAA-9, NOAA-10, NOAA-11, NOAA-12, and NOAA-14). National Oceanic and Atmospheric Administration, Washington, DC.
- Knapp, K. R. and L. L. Stowe (2002), Evaluating the Potential for Retrieving Aerosol Optical Depth over Land from AVHRR Pathfinder Atmosphere Data, *J. Atmos. Sci.*, 59, 279–293, doi:10.1175/1520-0469(2002)059<0279:ETPFRA>2.0.CO;2.
- Lee, J., N. C. Hsu, A. M. Sayer, C. Bettenhausen, and P. Yang, AERONET-based nonspherical dust optical models and effects on the VIIRS Deep Blue/SOAR over-water aerosol product, *J. Geophys. Res.*, submitted.
- Levy, R. C., L. A. Remer, D. Tanré, Y. J. Kaufman, C. Ichoku, B. N. Holben, J. M. Livingston, P. B. Russell, and H. Maring (2003), Evaluation of the Moderate-Resolution Imaging Spectroradiometer (MODIS) retrievals of dust aerosol over the ocean during PRIDE, *J. Geophys. Res.*, 108, 8594, doi:10.1029/2002JD002460, D19.
- Levy, R. C., S. Mattoo, L. A. Munchak, L. A. Remer, A. M. Sayer, F. Patadia, and N. C. Hsu (2013), The Collection 6 MODIS aerosol products over land and ocean, *Atmos. Meas. Tech.*, 6, 2989–3034, doi:10.5194/amt-6-2989-2013.

- Liu, L., M. I. Mishchenko, I. Geogdzhayev, A. Smirnov, S. M. Sakerin, D. M. Kabanov, and O. A. Ershov (2004), Global validation of two-channel AVHRR aerosol optical thickness retrievals over the oceans, *J. Quant. Spect. Rad. Trans.*, 88(1-3), 97–109, doi: 10.1016/j.jqsrt.2004.03.031.
- Mei, L. L., Y. Xue, A. A. Kokhanovsky, W. von Hoyningen-Huene, G. de Leeuw, and J. P. Burrows (2014), Retrieval of aerosol optical depth over land surfaces from AVHRR data, *Atmos. Meas. Tech.*, 7, 2411–2420, doi:10.5194/amt-7-2411-2014.
- Mishchenko, M.I., L.D. Travis, R.A. Kahn, and R.A. West, (1997) Modeling phase functions for dustlike tropospheric aerosols using a mixture of randomly oriented polydisperse spheroids. *J. Geophys. Res.*, 102, 16831–16847, doi:10.1029/96JD02110.
- Mishchenko, M. I., I. V. Geogdzhayev, B. Cairns, W. B. Rossow, and A. A. Lacis (1999), Aerosol retrievals over the ocean by use of channels 1 and 2 AVHRR data: sensitivity analysis and preliminary results, *Appl. Opt.*, 38(36), 7325–7341, doi:10.1364/AO.38.007325.
- Rao, C. R. N., L. L. Stowe, and E. P. McClain (1989), Remote sensing of aerosols over the oceans using AVHRR data: Theory, practice and applications, *Int. J. Remote Sens.*, 10(4-5), 743–749, doi:10.1080/01431168908903915.
- Riffler, M., C. Popp, A. Hauser, F. Fontana, and S. Wunderle (2010), Validation of a modified AVHRR aerosol optical depth retrieval algorithm over Central Europe, *Atmos. Meas. Tech.*, 3, 1255–1270, doi:10.5194/amt-3-1255-2010.
- Sayer, A. M., N. C. Hsu, C. Bettenhausen, Z. Ahmad, B. N. Holben, A. Smirnov, G. E. Thomas, and J. Zhang (2012a), SeaWiFS Ocean Aerosol Retrieval (SOAR): Algorithm, validation, and comparison with other data sets, *J. Geophys. Res.*, 117, D03206, doi:10.1029/2011JD016599.
- Sayer, A. M., Hsu, N. C., Bettenhausen, C., Jeong, M.-J., Holben, B. N., and Zhang (2012b), J., Global and regional evaluation of over-land spectral aerosol optical depth retrievals from SeaWiFS, *Atmos. Meas. Tech.*, 5, 1761–1778, doi:10.5194/amt-5-1761-2012.
- Sayer, A. M., A. Smirnov, N. C. Hsu, and B. N. Holben (2012c), A pure marine aerosol model, for use in remote sensing applications, *J. Geophys. Res.*, 117, D05213, doi:10.1029/2011JD016689.
- Sayer, A. M., A. Smirnov, N. C. Hsu, L. A. Munchak, and B. N. Holben (2012d), Estimating marine aerosol particle volume and number from Maritime Aerosol Network data, *Atmos. Chem. Phys.*, 12, 8889–8909, doi:10.5194/acp-12-8889-2012.
- Sayer, A. M., N. C. Hsu, C. Bettenhausen, and M.-J. Jeong (2013), Validation and uncertainty estimates for MODIS Collection 6 "Deep Blue" aerosol data, *J. Geophys. Res.*, 118, 7864–7872, doi:10.1002/jgrd.50600.
- Sayer, A. M., Hsu, N. C., Bettenhausen, C., Holz, R. E., Lee, J., Quinn, G., and Veglio, P. (2017a), Cross- calibration of S-NPP VIIRS moderate-resolution reflective solar bands against

MODIS Aqua over dark water scenes, *Atmos. Meas. Tech.*, 10, 1425–1444, doi:10.5194/amt-10-1425-2017.

Sayer, A. M., N. C. Hsu, J. Lee, N. Carletta, S.-H. Chen, and A. Smirnov (2017b), Evaluation of NASA Deep Blue/SOAR aerosol retrieval algorithms applied to AVHRR measurements, *J. Geophys. Res.*, submitted.

Seidel, F. C. and C. Popp (2012), Critical surface albedo and its implications to aerosol remote sensing, *Atmos. Meas. Tech.*, 5, 1653–1665, doi:10.5194/amt-5-1653-2012.

Smirnov, A., B. N. Holben, T. F. Eck, O. Dubovik, and I. Slutsker (2000), Cloud screening and quality control algorithms for the AERONET database, *Remote Sens. Environ.*, 73 (3), 337–349, doi: 10.1016/S0034-4257(00)00109-7.

Smirnov, A., Holben, B. N., Giles, D. M., Slutsker, I., O'Neill, N. T., Eck, T. F., Macke, A., Croot, P., Courcoux, Y., Sakerin, S. M., Smyth, T. J., Zielinski, T., Zibordi, G., Goes, J. I., Harvey, M. J., Quinn, P. K., Nelson, N. B., Radionov, V. F., Duarte, C. M., Losno, R., Sciare, J., Voss, K. J., Kinne, S., Nalli, N. R., Joseph, E., Krishna Moorthy, K., Covert, D. S., Gulev, S. K., Milinevsky, G., Larouche, P., Belanger, S., Horne, E., Chin, M., Remer, L. A., Kahn, R. A., Reid, J. S., Schulz, M., Heald, C. L., Zhang, J., Lapina, K., Kleidman, R. G., Griesfeller, J., Gaitley, B. J., Tan, Q., and Diehl, T. L. (2011), Maritime aerosol network as a component of AERONET – first results and comparison with global aerosol models and satellite retrievals, *Atmos. Meas. Tech.*, 4, 583–597, doi:10.5194/amt-4-583-2011.

Spurr, R. J. D. (2006), VLIDORT: A linearized pseudo-spherical vector discrete ordinate radiative transfer code for forward model and retrieval studies in multilayer multiple scattering media, *J. Quant. Spectros. Radiat. Transfer*, 102(2), 316–342, doi:10.1016/j.jqsrt.2006.05.005.

Stowe, L. L., A. M. Ignatov, and R. R. Singh (1997), Development, validation and potential enhancements to the second generation operational aerosol product at NOAA/NESDIS, *J. Geophys. Res.*, 102 (D14) 16923–16934, doi:10.1029/96JD02132.

Tanré, D., B. N. Holben, and Y. J. Kaufman (1992), Atmospheric correction algorithm for NOAA-AVHRR products: theory and application, *IEEE Trans. Geosci. Remote Sens.*, 30(2), 231–248, doi:10.1109/36.134074.

Tanré, D., Y. J. Kaufman, M. Herman, and S. Mattoo (1997), Remote sensing of aerosol properties over oceans using the MODIS/EOS spectral radiances, *J. Geophys. Res.*, 102 (D14), 16,971–16,988, doi:10.1029/96JD03437.

Tucker, C. J. (1979), Red and photographic infrared linear combinations for monitoring vegetation, *Remote Sens. Environ.*, 8, 127–150, doi:10.1016/0034-4257(79)90013-0.

Tucker, C. J., Pinzon, J. E., Brown, M.E., Slayback, D. A., Pak, E. W., Mahoney, R., Vermote, E. R., and N. El Saleous (2005), An extended AVHRR 8-km NDVI dataset compatible with

- MODIS and SPOT vegetation NDVI data, *Int. J. Remote Sens.*, 26(20):4485–4498, doi:10.1080/01431160500168686.
- Vermote, E. and Y. J. Kaufman (1995), Absolute calibration of AVHRR visible and near-infrared channels using ocean and cloud views, *Int. J. Remote Sens.*, 16(13), 2317–2340, doi:10.1080/01431169508954561.
- Wu, X., J. T. Sullivan, and A. K. Heidinger (2010), Operational calibration of the Advanced Very High Resolution Radiometer (AVHRR) visible and near-infrared channels, *Can. J. Remote Sens.*, 36(5), 602–616, doi:10.5589/m10-080.
- Yoon, J. M., J. Kim, J. H. Lee, H. K. Cho, B. J. Sohn, and M. H. Ahn (2007), Retrieval of aerosol optical depth over East Asia from a geostationary satellite, MTSAT-1R, Asia-Pac, *J. Atmos. Sci.*, 43, 133–142, doi:10.1063/1.3116999.
- Zhang, H., S. Kondragunta, I. Laszlo, H. Liu, L. A. Remer, J. Huang, S. Superczynski, and P. Ciren (2016), An enhanced VIIRS aerosol optical thickness (AOT) retrieval algorithm over land using a global surface reflectance ratio database, *J. Geophys. Res. Atmos.*, 121, 10,717–10,738, doi:10.1002/2016JD024859.
- Zhao, X., L. L. Stowe, A. Smirnov, D. Crosby, J. Sapper, and C. R. McClain (2002), Development of a global validation package for satellite oceanic aerosol optical thickness retrieval based on AERONET observations and its application to NOAA/NESDIS operational aerosol retrievals, *J. Atmos. Sci.*, 59, 294–312, doi:10.1175/1520-0469(2002)059<0294:DOAGVP>2.0.CO;2.
- Zhao, T. X.-P., I. Laszlo, O. Dubovik, B. N. Holben, J. Sapper, D. Tanré, and C. Pietras (2003), A study of the effect of non-spherical dust particles on the AVHRR aerosol optical thickness retrievals, *Geophys. Res. Lett.*, 30, 1317, doi:10.1029/2002GL016379.
- Zhao, T. X.-P., O. Dubovik, A. Smirnov, B. N. Holben, J. Sapper, C. Pietras, K. J. Voss, and R. Frouin (2004), Regional evaluation of an advanced very high resolution radiometer (AVHRR) two-channel aerosol retrieval algorithm, *J. Geophys. Res.*, 109, D02204, doi:10.1029/2003JD003817.

Table 1. AVHRR channel names, approximate ranges of peak spectral response, and shorthand for central wavelengths indicated in this study. Note channel 3A is only present on the AVHRR/3 sensors (NOAA15 onwards).

Number	Range of peak spectral response (μm)	Shorthand
1	0.58-0.68	630 nm
2	0.72-1.0	850 nm
3a	1.58-1.64	1.6 μm
3b	3.55-3.93	3.7 μm
4	10.30-11.30	11 μm
5	11.50-12.50	12 μm

Table 2. Aerosol optical model, AOD ranges, FMF values, size distribution parameters, refractive indices, and references for the AVHRR application of SOAR. For each model fine mode parameters are on the first line and coarse the second.

Model	Reference	FMF	AOD range	Modal radius, μm	Spread	Refractive index (550, 630, 840 nm)
Dust	Lee et al (2017)	0.1	0.15-5.0	0.19	0.44	1.430-0.001 <i>i</i> , 1.430-0.001 <i>i</i> , 1.430-0.001 <i>i</i>
				2.0	0.51	1.543-0.0012 <i>i</i> , 1.543-0.0009 <i>i</i> , 1.521-0.0006 <i>i</i>
Fine-dominated	Sayer et al (2012a)	0.8	0.2-3.5	0.19	0.44	1.430-0.0075 <i>i</i> , 1.430-0.0075 <i>i</i> , 1.430-0.0075 <i>i</i>
				2.75	0.65	1.363-0 <i>i</i> , 1.363-0 <i>i</i> , 1.363-0 <i>i</i>
Marine, 1	Sayer et al (2012a,c)	0.5	0.001-0.2	0.157	0.5	1.414-0.0021 <i>i</i> , 1.413-0.0025 <i>i</i> , 1.408-0.0035 <i>i</i>
				2.59	0.72	1.361-0 <i>i</i> , 1.358-0 <i>i</i> , 1.357-0 <i>i</i>
Marine, 2	Sayer et al (2012a,c)	0.7	0.001-0.2	0.157	0.5	1.414-0.0021 <i>i</i> , 1.413-0.0025 <i>i</i> , 1.408-0.0035 <i>i</i>
				2.59	0.72	1.361-0 <i>i</i> , 1.358-0 <i>i</i> , 1.357-0 <i>i</i>

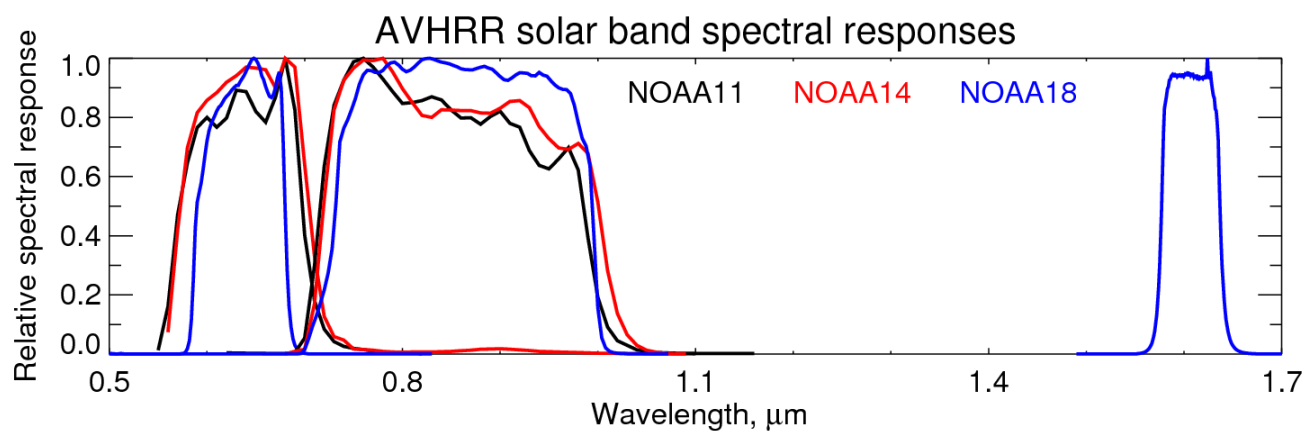


Figure 1. Solar band spectral response functions for AVHRR/2 on NOAA11 (black), NOAA14 (red), and AVHRR/3 on NOAA18 (blue). Spectral response functions are available from https://www.star.nesdis.noaa.gov/smcd/spb/fwu/homepage/AVHRR/spec_resp_func/index.html.

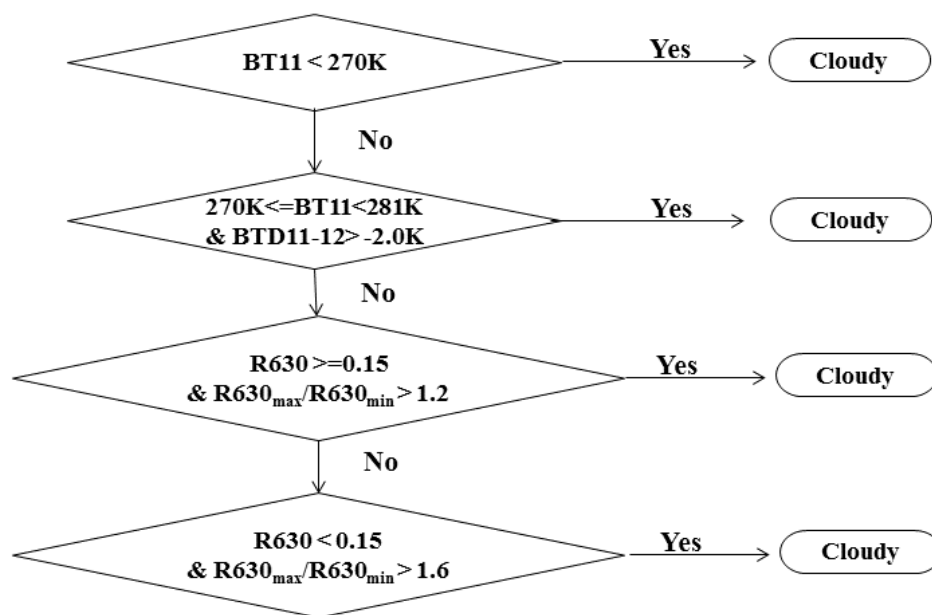


Figure 2. Schematic diagram of cloud screening scheme used in the AVHRR Deep Blue over-land algorithm. Acronyms indicate brightness temperatures (BT), BT differences (BTD), and reflectances (R) at channel wavelengths denoted. Subscripts max and min refer to the maximum and minimum values within the 3x3 pixel area.

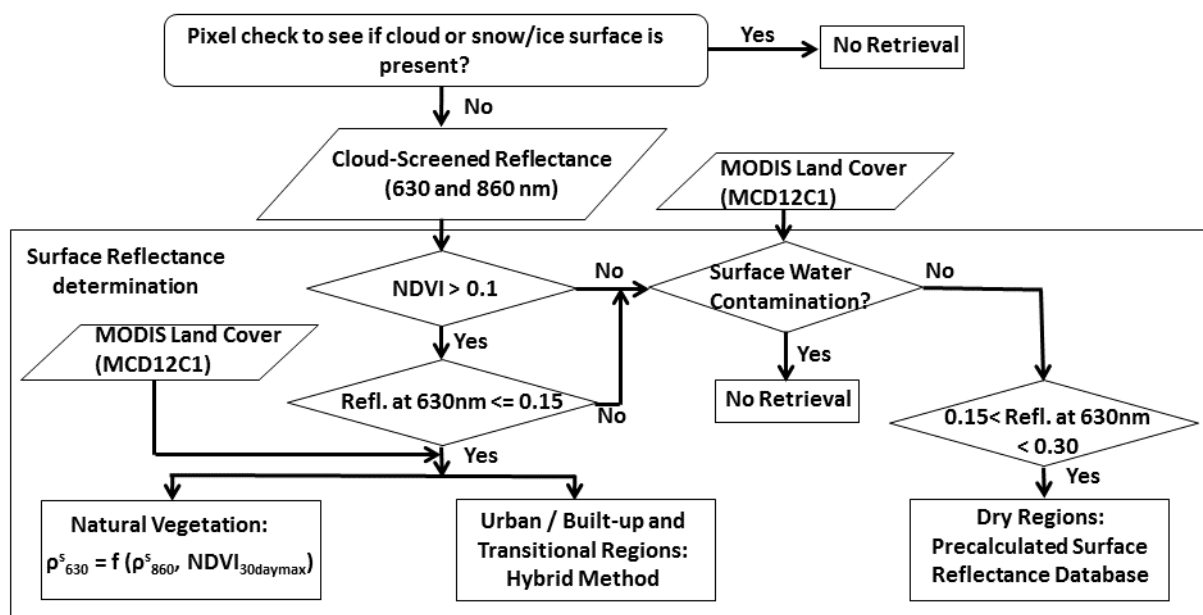


Figure 3. Flowchart of the AVHRR Deep Blue land surface reflectance determination scheme.

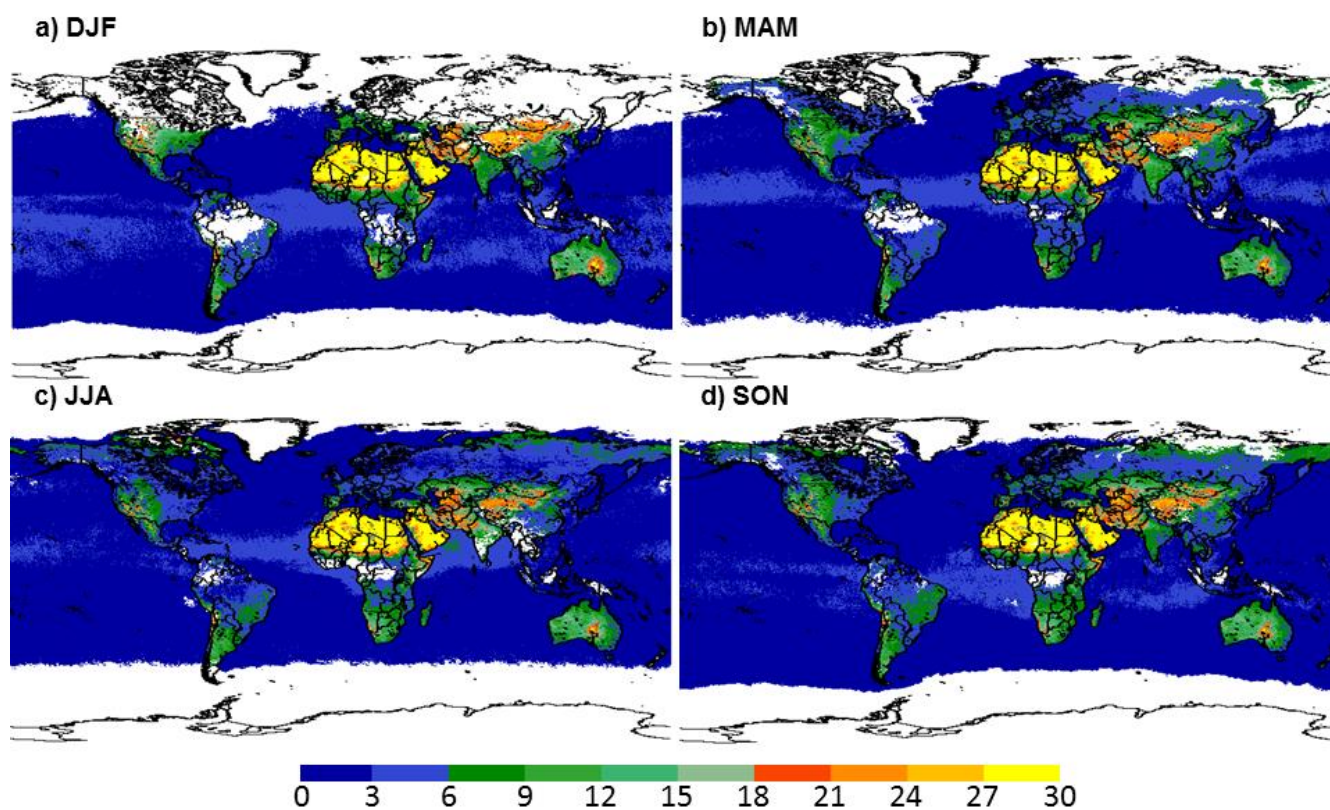
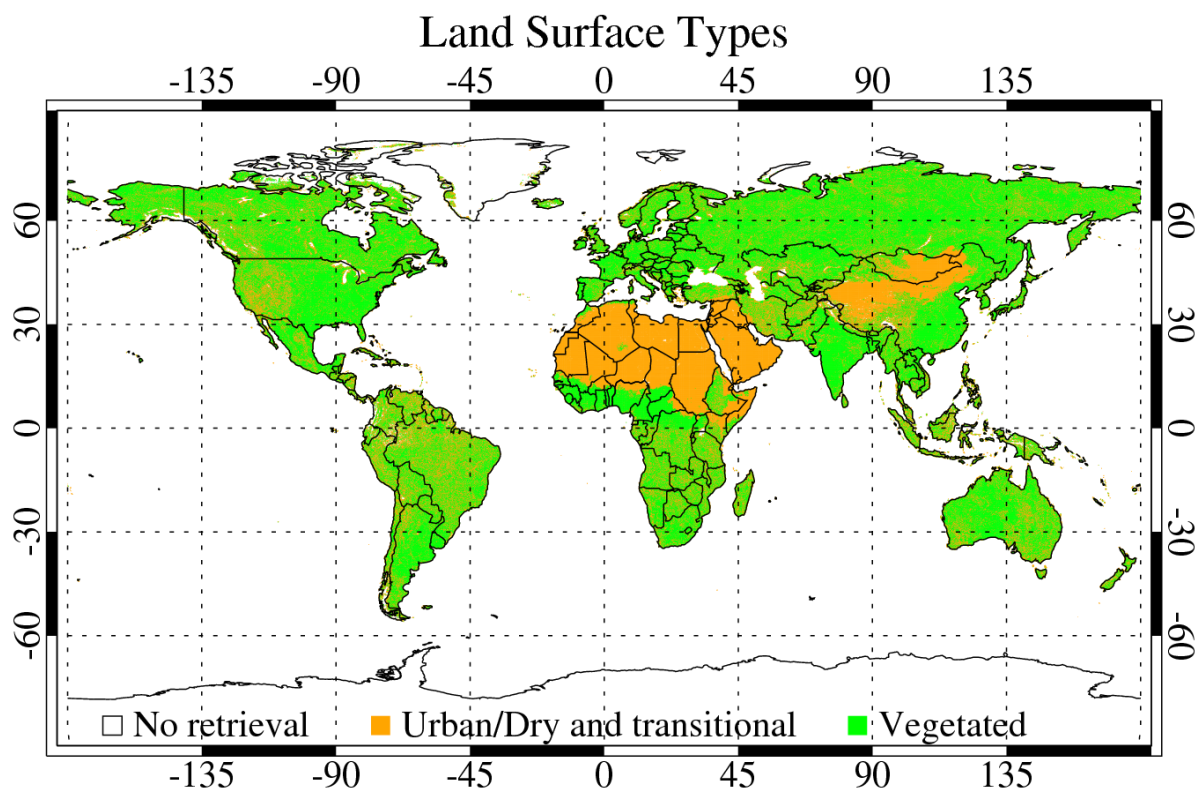


Figure 4. Seasonal maps of NOAA-18 AVHRR surface database showing reflectance (%) at band 1 (630 nm) for (a) December-February, (b) March-May, (c) June-August, and (d) September-November. Grid cells without a valid value are indicated in white.



973
 974 Figure 5. Land surface types showing where each surface reflectance approach is applied. The seasonal
 975 surface reflectance database with scattering angle dependence is used for urban, dry, or transitional land
 976 surfaces (orange), and 30-day maximum NDVI database is used for vegetated surfaces (green).

977

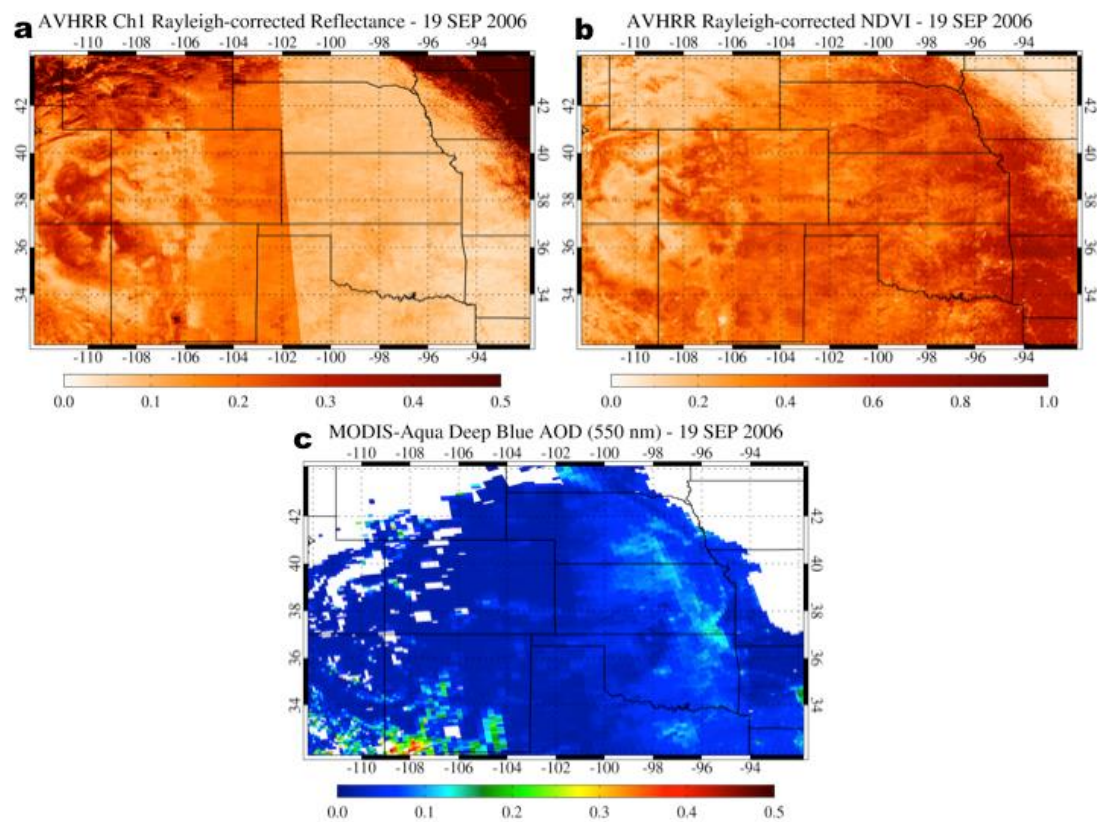


Figure 6. (a) AVHRR band 1 (630 nm) Rayleigh-corrected TOA reflectance, and (b) Rayleigh-corrected NDVI, and (c) MODIS Aqua Deep Blue AOD at 550 nm over part of the U.S. on 19 September 2006.

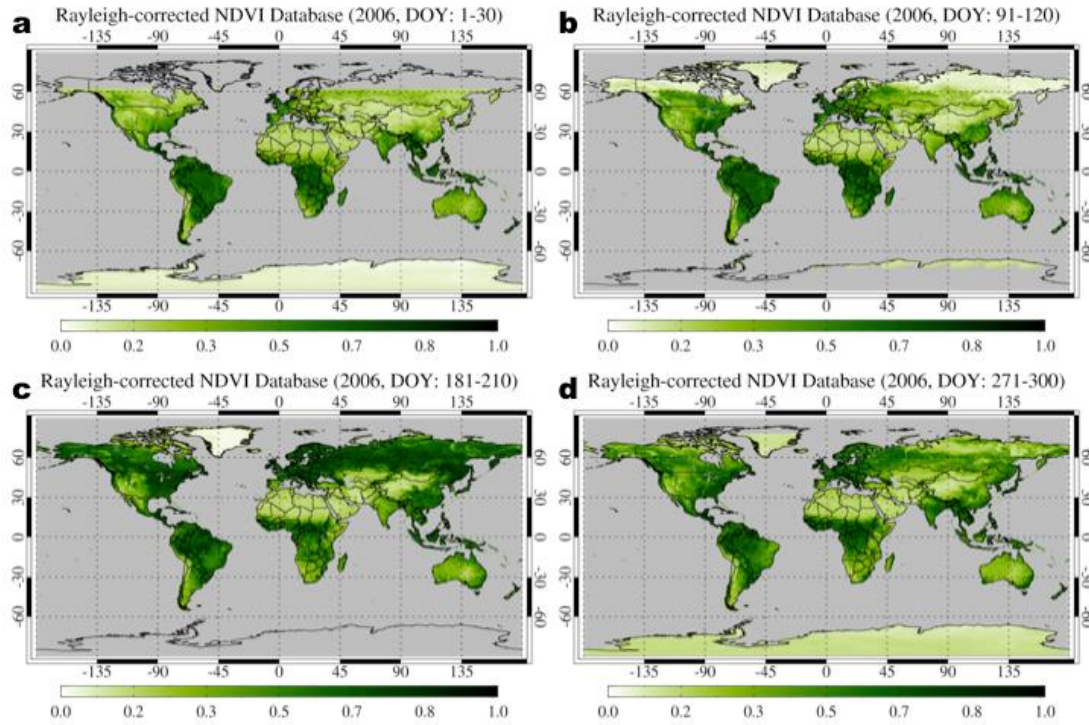


Figure 7. Maximum Rayleigh-corrected NDVI in four 30-day windows in 2006. Day of year windows for each plot are (a) 1-30, (b) 91-120, (c) 181-210, and (d) 271-300, representative of boreal winter, spring, summer, and fall respectively.

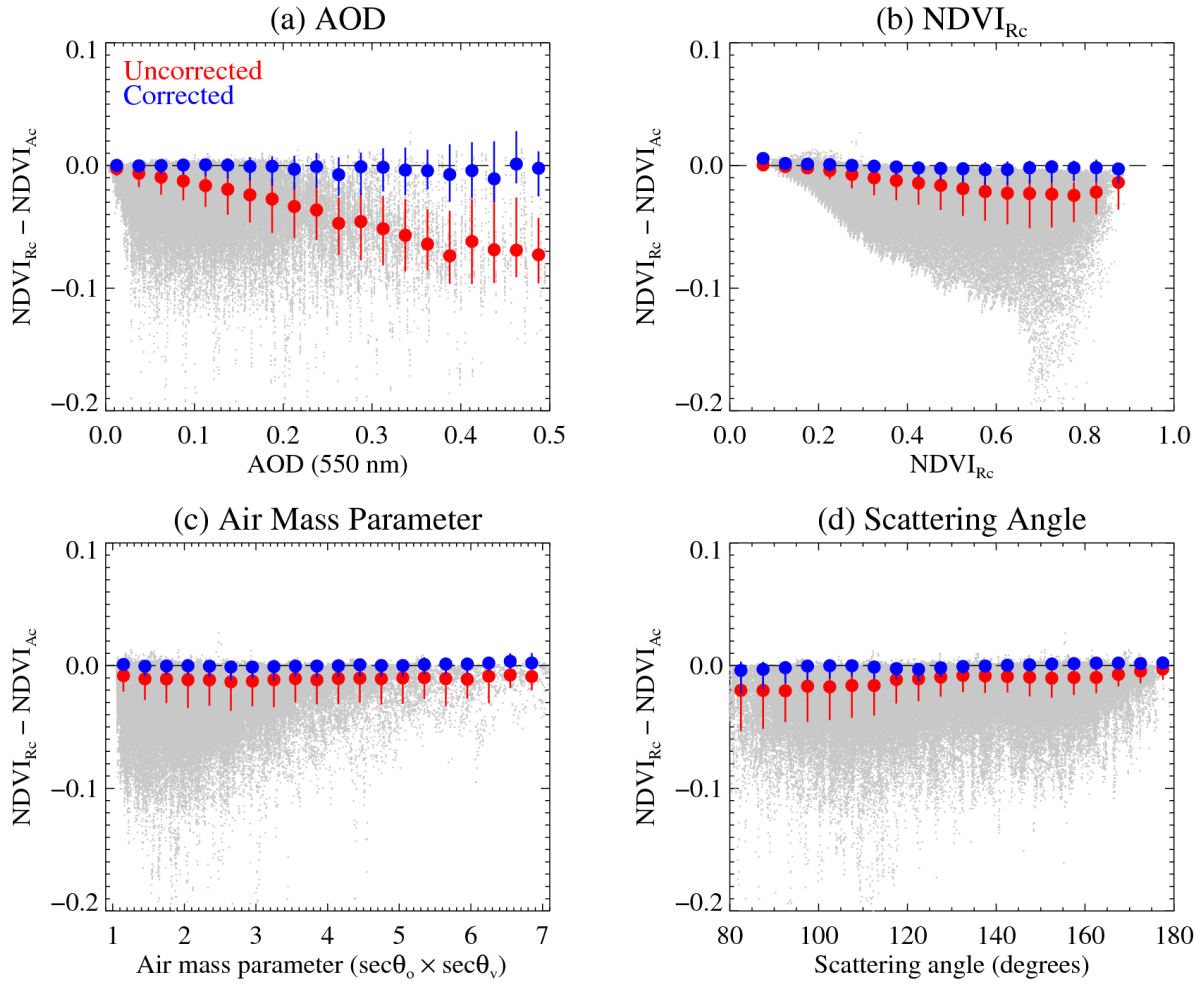


Figure 8. Median and central 68% interval of the difference between Rayleigh-corrected NDVI ($NDVI_{Rc}$) and atmosphere-corrected NDVI ($NDVI_{Ac}$) as a function of (a) 550 nm AOD, (b) $NDVI_{Rc}$, (c) air mass parameter, and (d) scattering angle for the period from 2006 to 2011 before (red) and after (blue) the correction of aerosol signals in $NDVI_{Rc}$. Gray dots show individual data points used for the uncorrected data. All North American AERONET sites available for the test period are used for this analysis.

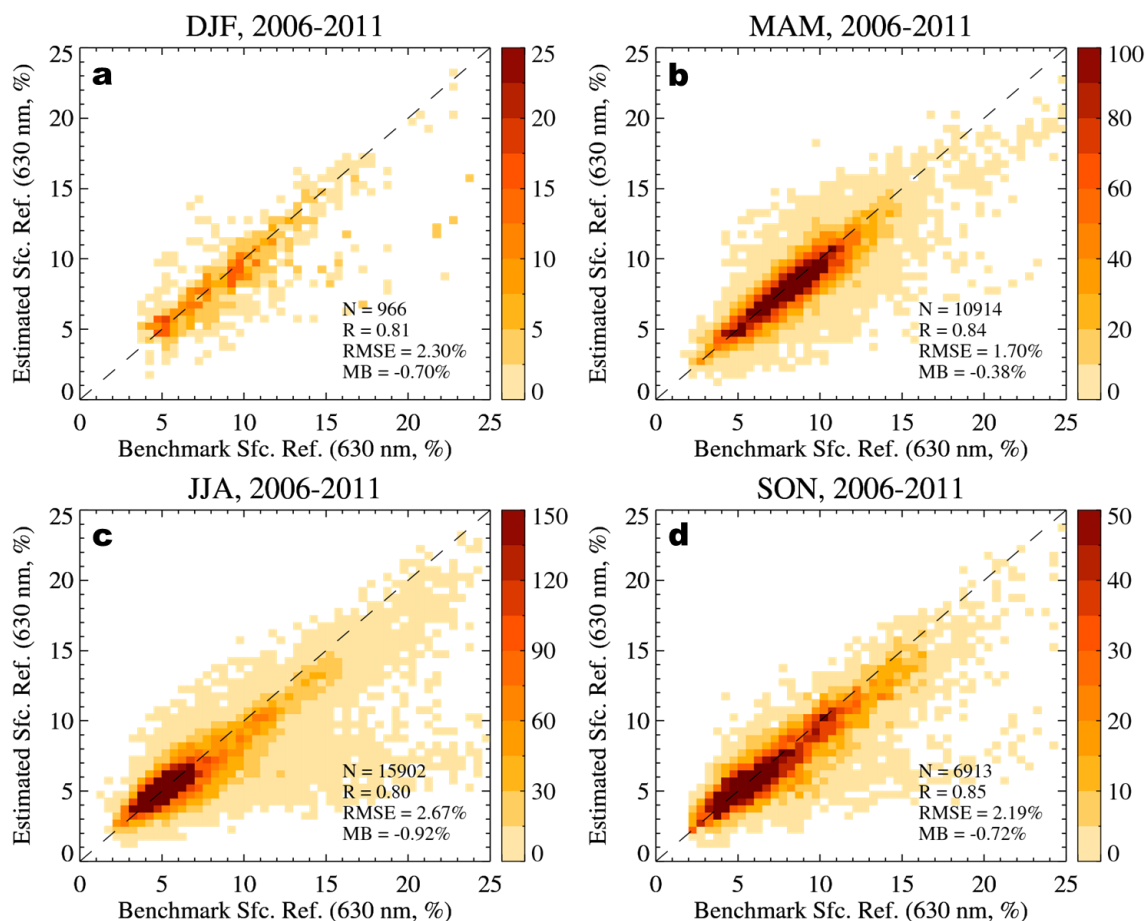


Figure 9. Scatter density plots between benchmark surface reflectance (atmospherically-corrected TOA reflectance) and estimated surface reflectance from the maximum NDVI database over North America in each season from 2006 to 2011. Statistics shown are the number of data points (N), Pearson coefficient (R), root-mean-square error (RMSE), and mean bias (MB).

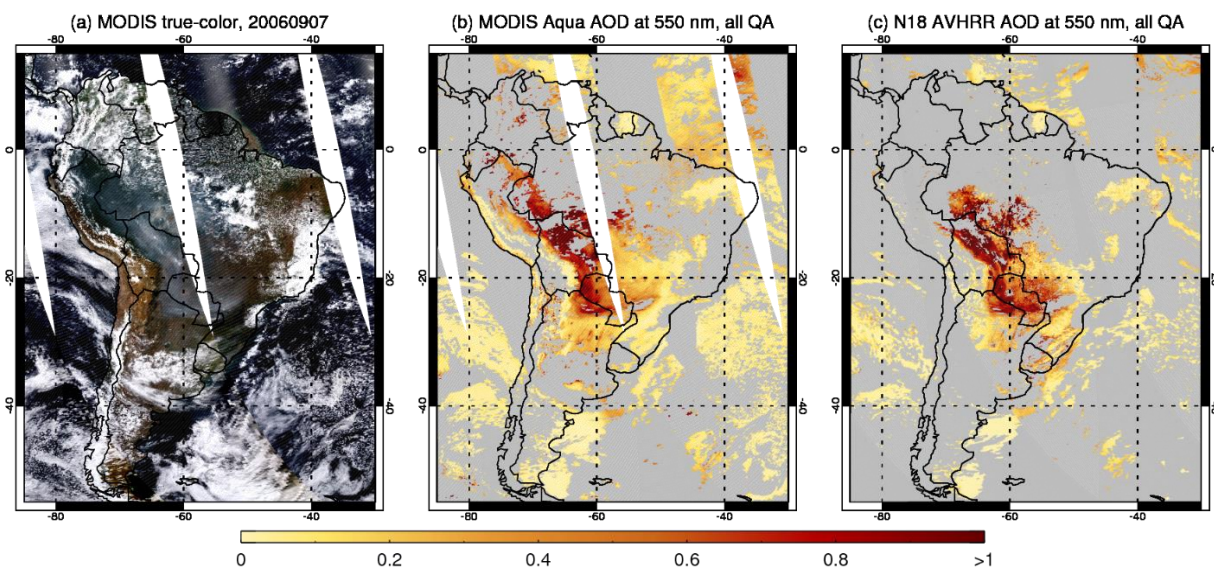


Figure 10. (a) MODIS Aqua true-color image, (b) MODIS AOD at 550 nm from Collection 6, and (c) the new AVHRR AOD at the same wavelength from NOAA18, for a smoke event over South America on 7 September 2006.

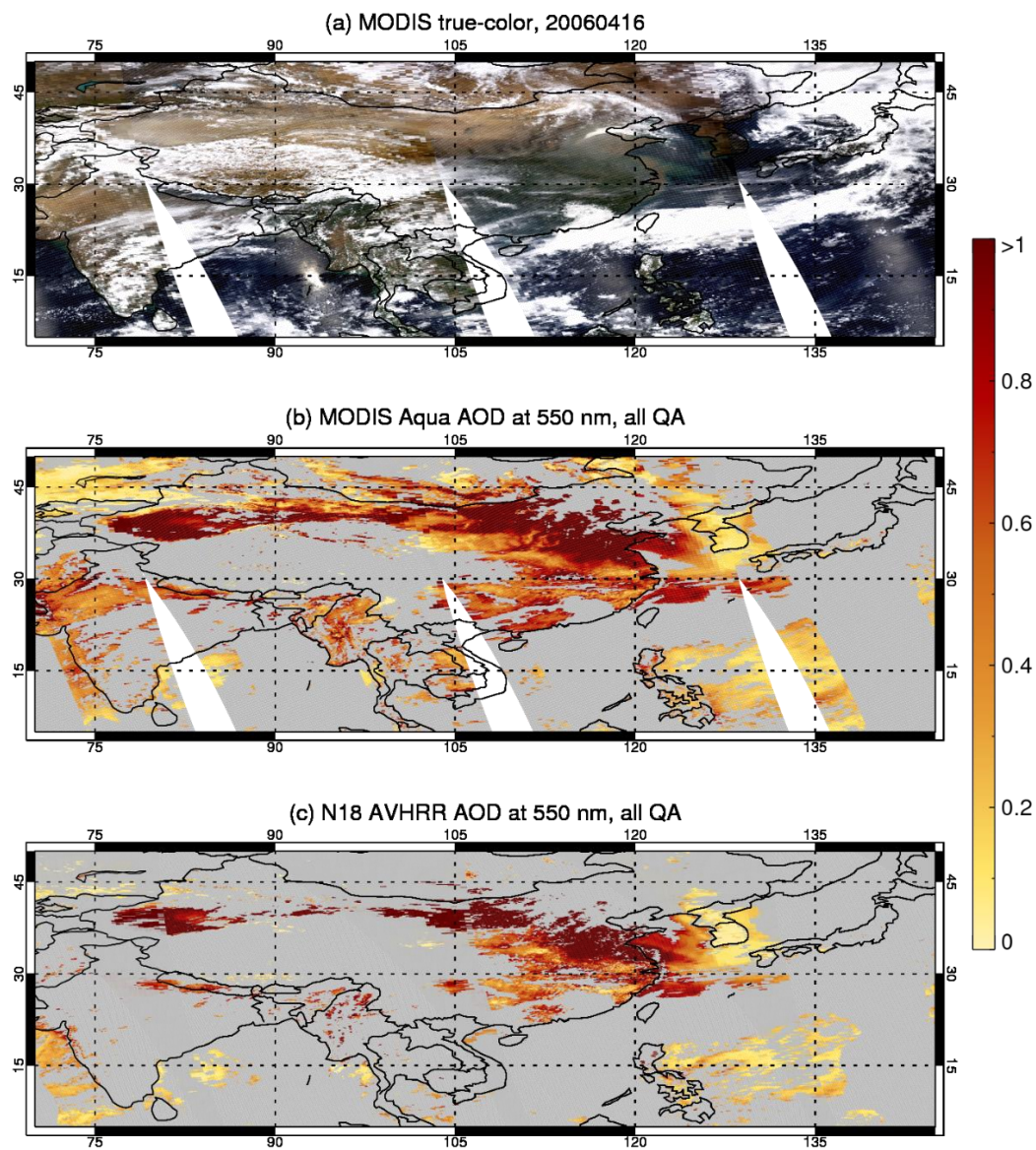


Figure 11. As Figure 10, except for a heavy dust/pollution mixture event over Asia on 16 April 2006.

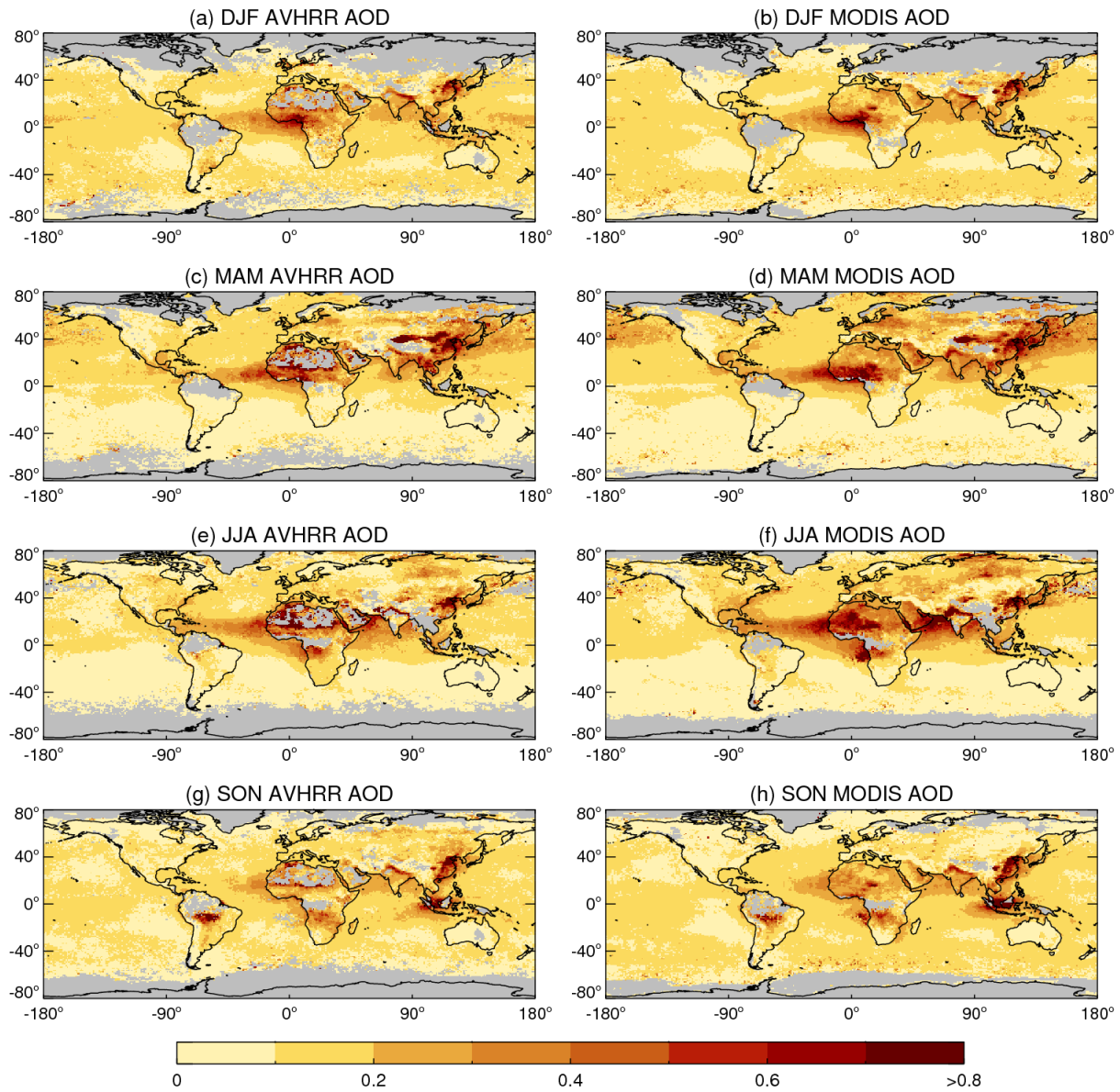


Figure 12. Seasonal composites of NOAA-18 AVHRR (left) and MODIS Aqua (right) AOD at 550 nm for the year 2006. Grid cells without sufficient data (see text) are shaded in grey.

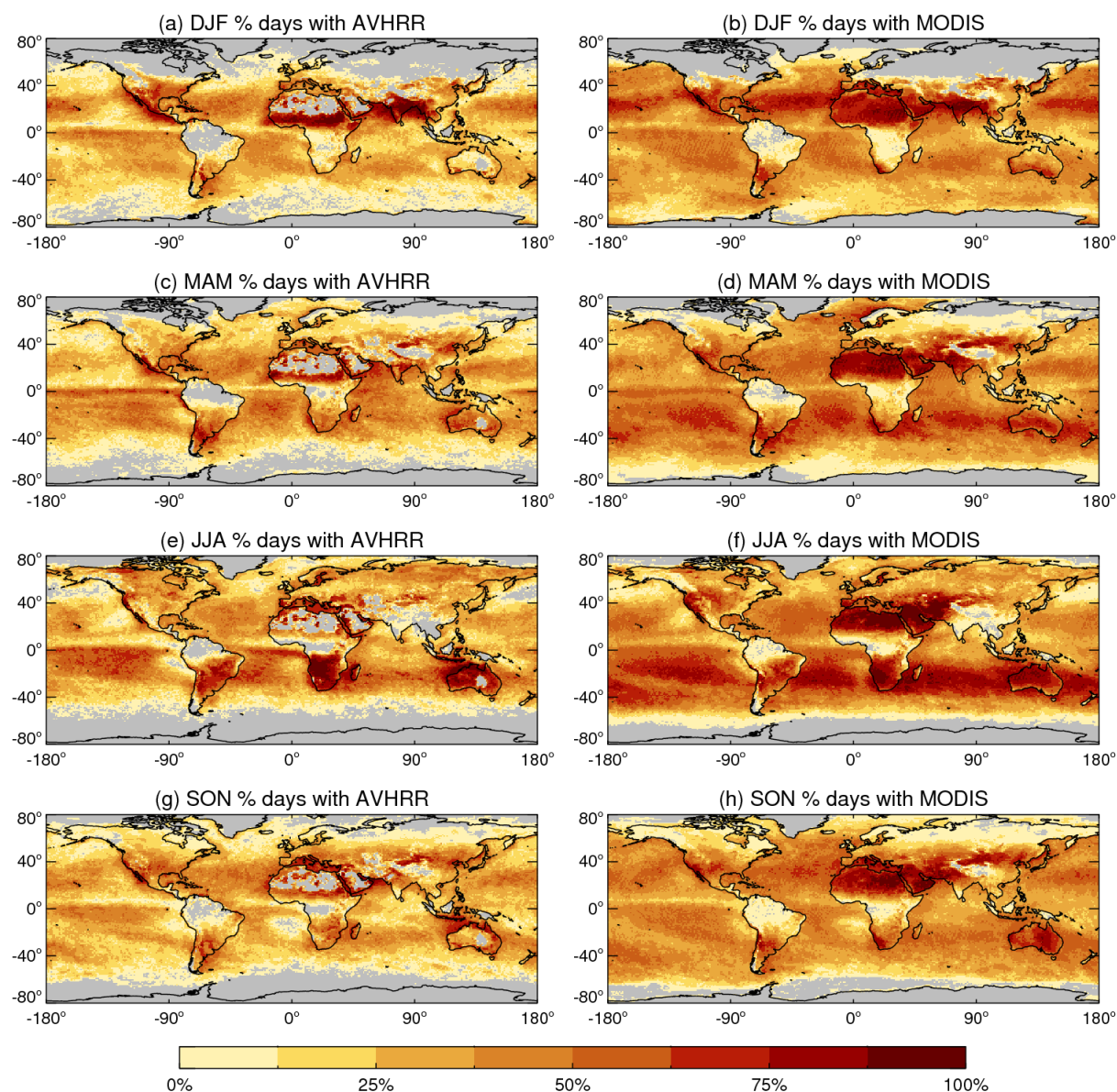


Figure 13. As Figure 12, except for showing the percentage of days within each season containing sufficient AOD data for the Level 3 grid cells to be populated (see text).

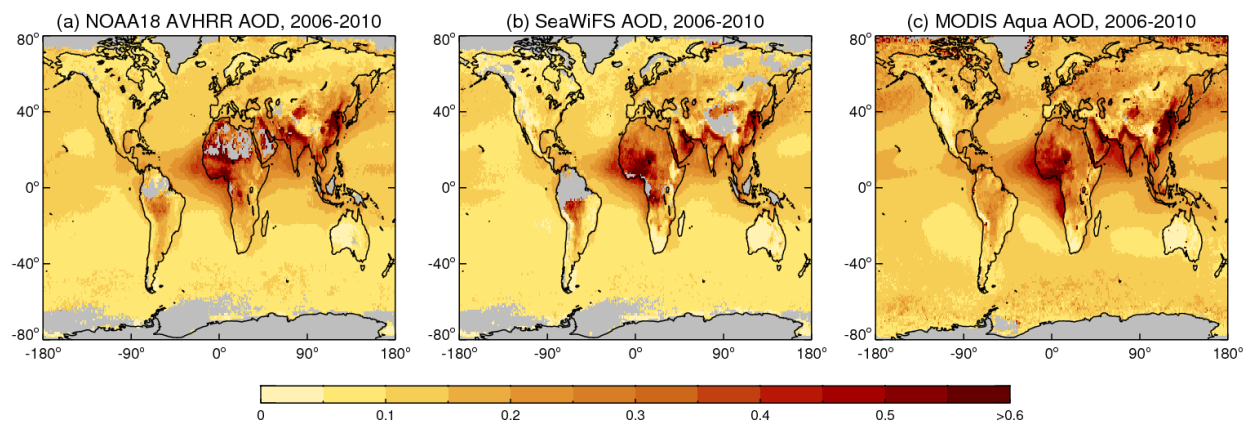
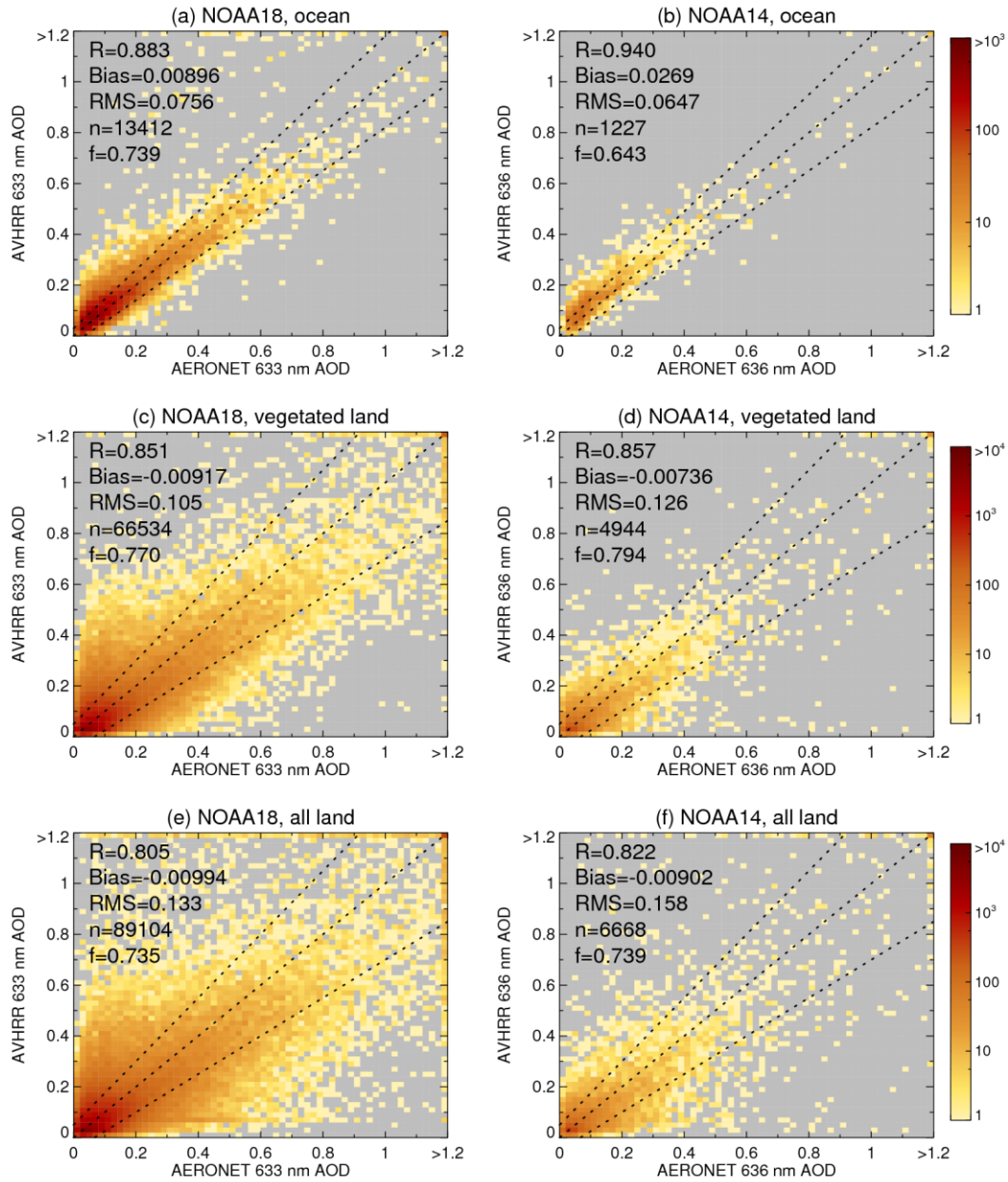


Figure 14. Multiannual mean composites of AOD at 550 nm, for (a) NOAA18 AVHRR, (b) SeaWiFS, and (c) MODIS Aqua, for their common overlap period (2006-2010). Grid cells with fewer than 24 months during this period containing valid monthly mean data are shaded in grey.



1031

1032 Figure 15. Scatter density histograms between AERONET and AVHRR AOD at band 1. Data are

1033 shown separately for (a, c, e) NOAA18 and (b, d, f) NOAA14, for (a, b) SOAR ocean retrievals,

1034 (c, d) Deep Blue land retrievals for vegetated scenes, and (e, f) all Deep Blue land retrievals.

1035 Dashed lines indicate the expected error (EE) envelopes of $\pm(0.03+15\%)$ over water and1036 $\pm(0.05+25\%)$ over land, respectively. Statistics indicate the correlation coefficient (R), median

1037 (AVHRR-AERONET) bias, root mean square (RMS) error, data count (n), and fraction of points
1038 matching within the EE (*f*).
1039
1040